Electronic Supplementary Material (ESI) for Energy & Environmental Science.
This journal is © The Royal Society of Chemistry 2018

Two-Dimensional Materials in Semiconductor Photoelectrocatalytic Systems for Water Splitting

Monireh Faraji[a,b1], Mahdieh Yousefi[c1], Samira Yousefzadeh[d], Mohammad Zirak[e], Naeimeh Naseri[a], Tae Hwa Jeon[f], Wonyong Choi,[f2]. Alireza Z. Moshfegh[a,c2]

[a]*Department of Physics, Sharif University of Technology, P.O. Box 11555-9161, Tehran, Iran*

[b]*Chemistry Faculty, North Tehran Branch, Islamic Azad University, P.O.Box 16511-53311, Tehran, Iran*

[c] *Institute for Nanoscience and Nanotechnology, Sharif University of Technology, P.O. Box 14588-8969, Tehran, Iran*

[d] *Department of Physics, Faculty of Science, Sahand University of Technology, P.O. Box 51335-1996, Tabriz, Iran*

[e] *Department of Physics, Hakim Sabzevari University, P. O. Box 961797648, Sabzevar, Iran*

[f.] *School of Environmental Science and Engineering, Pohang University of Science and Technology (POSTECH), Hyoja-dong, Pohang, Korea*

---

[1] *These authors are equal main contributor*

[2] *Corresponding authors, email address : moshfegh@sharif.edu, wchoi@postech.edu*

Contents

1 PEC principles *3*

2 2D/Semiconductor interface study tool box *6*

2.1 Morphological/structural diagnosis **6**

2.1.1 Scanning electron microscopy (SEM) 6

2.1.2 High resolution transmission electron microscopy (HRTEM) 7

2.1.3 Atomic Force Microscopy (AFM) 7

2.1.4 X-ray diffraction 8

2.1.5 Raman Spectroscopy 10

2.2 Optical/Electrical diagnosis **12**

2.2.1 Ultra violet photoelectron spectroscopy (UPS) 13

2.2.2 Photoluminescence spectroscopy 14

2.3 Photoelectrochemical investigation **15**

2.3.1 Photoresponse 15

2.3.2 Impedance and Mott–Schottky Analysis 20

2.4 Theoretical insight **23**

2.4.1 Optical absorption spectra: 24

2.4.2 Electronic structure calculation 24

2.4.3 Charge transport analysis 25

3 2D materials in brief *27*

3.1 graphene **27**

3.2 Transition metal dichalcogenides **29**

3.3 *g*-C_3N_4 ..... **32**

1 PEC principles

A simple photoelectrochemical cell consists of three components including a semiconductor (SC) photoanode/ photocathode (n-type/p-type), a metal counter electrode (usually Pt), and aqueous electrolyte in which the photoanode and counter electrode are immersed in the solution[1]. The process of water splitting can be envisaged as two half reactions namely as water oxidation to dioxygen and proton reduction to hydrogen. When the semiconductor is illuminated by photons with energies (hν) equal to or higher than the bandgap energy, electron-hole pairs are generated under this circumstance. To split water efficiently, these photoinduced electrons and holes are spatially separated due to the presence of built-in electric field inside the semiconductor with transporting electrons to the metal counter electrode through an external circuit. At the surface of metal electrode, water is reduced by photogenerated electrons to form hydrogen gas, while at the surface of semiconductor photoanode, water is oxidized by holes to produce oxygen gas[1-3].The reduction and oxidation reactions on each electrode can be expressed as below:

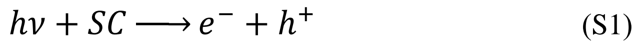

$$h\nu + SC \longrightarrow e^- + h^+ \quad \text{(S1)}$$

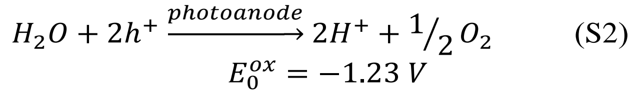

$$H_2O + 2h^+ \xrightarrow{photoanode} 2H^+ + {}^1/_2\, O_2 \quad \text{(S2)}$$
$$E_0^{ox} = -1.23\ V$$

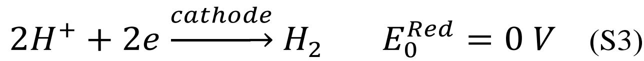

$$2H^+ + 2e \xrightarrow{cathode} H_2 \qquad E_0^{Red} = 0\ V \quad \text{(S3)}$$

The overall water splitting reaction is endothermic, confirmed by the Gibbs free energy change of +237 $kJmol^{-1}$ and therefore requires high overpotentials[1, 2]. As mentioned in above, light absorption, charge separation/migration, and surface chemical reactions are the three main steps for complete water splitting processes. In addition, the experimental efficiency of photon-to-hydrogen production (η) can be measured by J-V data in an n-type semiconductor photoelectrode and the efficiency can be estimated by the following equation:[4-6]

$$\eta = \frac{J_g \mu_{ex} \emptyset_{conv}}{S} \qquad \text{(S4)}$$

where J_g denotes the absorbed photon flux related to light absorption; μ_{ex} denotes the excess chemical potential to light absorption; $\emptyset_{conv}$ denotes the quantum yield for absorbed photons related to charge separation/migration and surface reaction and S denotes the total solar irradiance ($mW\ cm^{-2}$).

To optimize the overall PEC performance, it is important to understand the fundamental physics, thermodynamics, and kinetic parameters of semiconductor-electrolyte junction[6]. Since the photoelectrochemical cell is performed under light irradiation, steady-state illumination leads to non-equilibrium electron and hole populations and, in consequence, the single Fermi level (under dark condition) are split into holes and electrons quasi-Fermi levels, which can be used to describe the electrochemical potential of one carrier type on an individual basis, i.e. electrons or holes, under non-equilibrium conditions[4, 6]. When a semiconductor is brought into contact with electrolyte containing a redox couple, the photovoltage generated by the junction is controlled by the degree of splitting between quasi Fermi level of dominant carriers and Fermi level of the electrolyte. Depending on the type of semiconductor used for the PEC water splitting device, the desired redox couples are H^+/H_2 and O_2/ H_2O couple for the p-type and n-type semiconductor, respectively[6].

In Figure S1a, the charges transfer at the n-type semiconductor electrode/electrolyte junction, which occurs due to difference in positions between quasi-Fermi level of the semiconductor electrons and potential of the redox pair in electrolyte, leads to variation of charge distribution and, as a result, a region known as surface-charge layer is formed on each side of the junction. Thus on the electrolyte side, this region can be referred to as an electrical double layer, which encompasses Helmholtz layer (compact layer) and Gouy-Chapman layer (outer diffuse layer). Whereas on the semiconductor side, the formation of electric field is the main cause of band bending, the magnitude depends on the position of Fermi level in solid[6, 7]. The recombination of photo-generated charge carriers can be hindered by this electric field. Depending on the relative position between Fermi level of semiconductor and electrolyte potential, the space charge layer of n-type semiconductor can be classified into three types, namely as the accumulation layer, depletion layer, and inversion layer [4, 8]. The formation of accumulation layer is attributed to the accretion of mobile electrons near the surface in order to compensate excess positive charges adsorbed on the surface of n-type semiconductor. The depletion layer is the most common and important region within the space charge layer and can be formed when depletion of electrons develop from the solid into solution, leaving the layer in immobile ionized donor states. The inversion layer is formed when holes are accumulated in a thin layer on the surface[4, 9]. When a p-type semiconductor is used as a photoelectrode, similar processes occur under illumination condition (Figure S1b). However, in this case the positive holes are mobile charge carries, thus the solution near photoelectrode is positively charged. The thickness of space charge layer (L_{SC}) can be generally estimated by equations as follows[4].

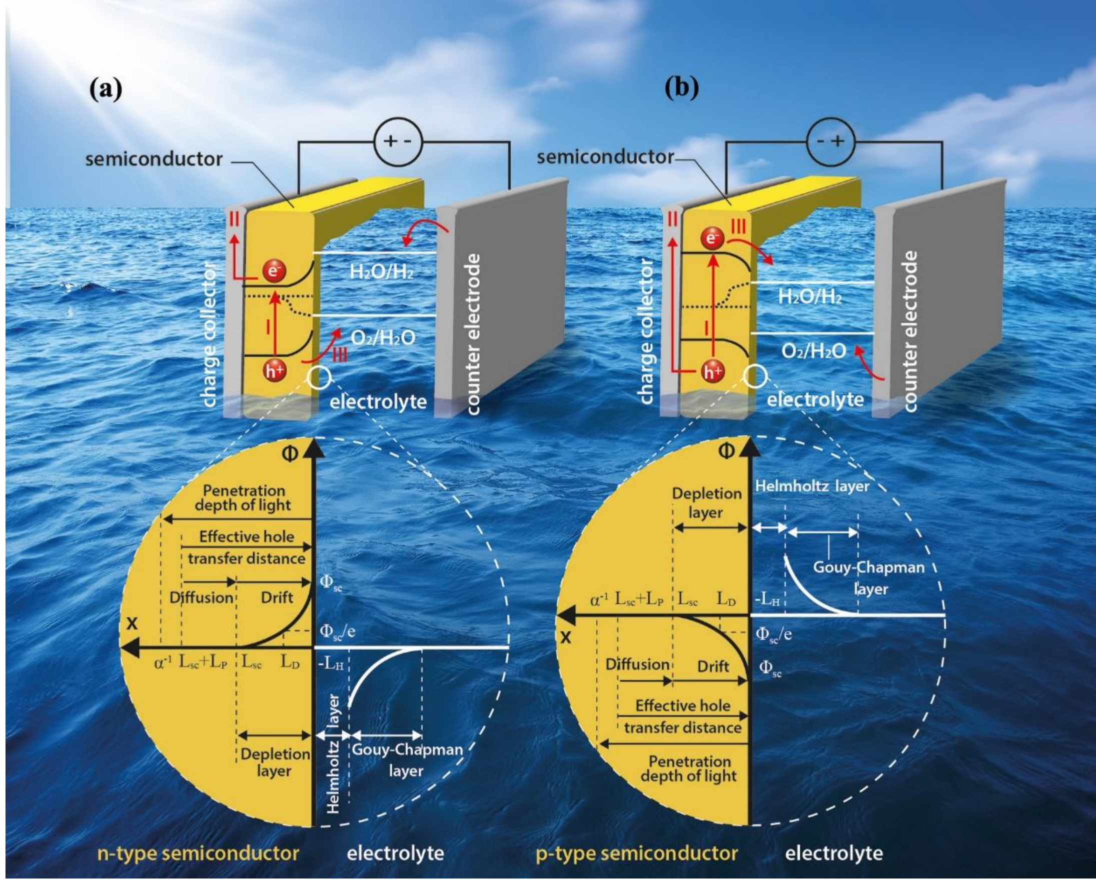

Figure S1. schematic diagram of semiconductor-based solar water splitting processes under illumination condition. (a) Simplified energy diagram for a photoanode (n-type semiconductor) and; (b) simplified energy diagram for a photocathode (p-type semiconductor). Adapted with permission from Ref. [4] (Copyright 2014 Elsevier).

$$L_{SC} = L_D \left[\frac{2q|\emptyset_{SC}|}{kT}\right]^{\frac{1}{2}} = L_D \left[\frac{2q(V - V_{fb})}{kT}\right]^{\frac{1}{2}} \quad \text{(S5)}$$

$$L_D = [\frac{\varepsilon_0 \varepsilon_r kT}{q^2(n_0 + p_0)}]^{1/2} \quad \text{(S6)}$$

where L_D, known as the Debye length, depends on the concentration of charge carriers in photoelectrode; ε_0 denotes the vacuum dielectric constant; ε_r denotes the relative dielectric constant for photoelectrode; k denotes the Boltzmann constant; T denotes in degrees Kelvin; V_{fb} denotes the flat band potential of the photoelectrode; and n_0 and p_0 denote the electron and hole concentration of the photoelectrode, respectively.

2 2D/Semiconductor interface study tool box

2.1 Morphological/structural diagnosis

2.1.1 Scanning electron microscopy (SEM)

Scanning electron microscopy (SEM) is a widely used technique to investigate the overall morphologies of various nanostructures. The modern scanning electron microscopes are also equipped with energy dispersive spectrometer (EDS). Therefore, elemental composition of the materials can also be analyzed as well as their morphology via SEM technique. High resolution SEM, known as field emission scanning electron microscope (FESEM), is cable to reveal the microstructure of multiple designed heterostructures. The morphology of many 2D-material/semiconductor heterostructures such as graphene-TiO_2 [10-13], graphene-ZnO [14-17], MoS_2-graphene[18, 19], MoS_2-TiO_2 [20], g-C_3N_4-MoS_2 [21], g-C_3N_4-TiO_2 [22], have been characterized via FESEM analysis. For example, the morphological information about MoS_2 nanosheets/S-doped g-C_3N_4 heterostructure grown on indium−tin oxide (ITO) substrate was obtained via SEM technique [21]. Figure S2(a1-a3) represents the top view and cross-sectional SEM images, as well as the corresponding EDS spectra of bare ITO, yellow CN film named m-CN/ITO (i.e., g-C_3N_4/ITO), transparent light yellow color smooth CN film named mt-CN/ITO (i.e., S-doped g-C_3N_4/ITO), and MoS_2/mt-CN/ ITO thin layers. For the m-CN/ITO sample, a very thin and uneven thick (<100 nm) layer was formed on the top of the 200 nm thick ITO layer (Figure S2 (b1-b3)). For SEM images of the mt-CN/ITO sample (Figure S2 (c1-c3)), the surface morphology clearly exhibits a unique lotus leaf-like structure containing some wrinkles. The MoS_2/mt-CN/ITO heterostructure (Figure S2 (d1-d3)) shows a coral-like surface structure, which is beneficial for photocatalytic activity due to its higher light energy capturing. Cross sectional SEM image of the MoS_2/mt-CN/ITO samples reveals that there is a mt-CN layer (thickness of about 50 nm) on the ITO substrate and a MoS_2 layer (average thickness of 100 nm) at the top of the sample. Corresponding EDS spectra Figure S2 (a4-d4)) show that the C, N, S, and Mo elements are all present in the samples[21].

As it was discussed earlier, the overall morphology of the 2D-material/semiconductor heterostructures can be investigated via SEM technique with high accuracy, but it is not possible to determine the nature of heterostructures interfaces via FESEM at the atomic scale, and more accurate techniques with higher resolution are required such as transition electron microscopy (TEM), which will be discussed in details in the following section.

2.1.2 High resolution transmission electron microscopy (HRTEM)

Electron-hole separation is one of the most important processes to enhance the PEC performance of a photo-active structure which occurs at the interface of the active materials. Formation of ultra-fine atomic junction between photo-active materials at their interface is a key step to achieve higher efficiency. Verification and observation of such atomic heterojunction can be achieved via TEM, particularly HRTEM. This technique is used for imaging and monitoring of the atomic structure of the materials and the atomic junctions at the interfaces directly. TEM uses very high energy electron beam (~100 keV) as imaging source where the electrons are transmitted through an ultra-thin specimen. Because of small de Broglie wavelength, electrons can interact with fine features of the material effectively when they transmit through it. This interaction provides an image which is magnified on an imagining device. If the magnification process is well constructed, the final image can show fine details even as small as a single column of atoms. HRTEM is extensively used to study the atomic structure of 2D materials especially their junction with other materials and also phase transition during various production and operation processes.

For determining different crystal structure (direct monitoring of atomic arrangement) and phases, HRTEM is a powerful tool. For example, a trigonal prismatic (2H) octahedral (1T) phase transition of MoS_2 nanosheets was directly observed and monitored during lithium intercalation process using HRTEM (Figure S2e and f)[23]. Figure S2e illustrates a HRTEM image of 2H-MoS_2 before lithiation. Figure S2f presents the HRTEM images of the same area after lithium ion intercalation which is clearly different from the Figure S2e and thus 2H-1T phase transition is directly observed and confirmed. Atomic heterojunctions between 2D materials with other structures can also be verified via HRTEM images[24, 25]. For example, the intimate 2D nano junction between MoS_2 and TiO_2 is clearly distinctable in Figure S2g. Such a clear observation confirms perfect atomic contact between TiO_2 and MoS_2 via their interface, which favors the photogenerated charge carrier separation and transfer through MoS_2/TiO_2 materials. These two important processes are key factors to understand the mechanism of charge transfer and thus photocatalytic activities of the 2D-2D MoS_2/TiO_2 heterostructure [25].

2.1.3 Atomic Force Microscopy (AFM)

AFM is a high-resolution scanning probe microscopy which was developed to extend scanning tunneling microscopy (STM) technique to investigate insulating surfaces with atomic resolution[26]. Atomic force microscopy is widely used to investigate the surface topography and surface morphology of the samples. Furthermore, by selecting an appropriate measurement mode and a suitable tip (insulating, conductive, magnetic, etc.), various physical and chemical surface properties can be extracted. When a conductive tip is used, the electrical potential can be applied between the tip and sample surface and the electrical current response is recorded (or vice versa). Therefore, the electrical nature of the surface can be investigated by

analyzing this data. As a result, AFM technique is capable of detecting the interface between two materials with different electrical conductivity. For example, the interface contact between graphene (conductive) and TiO_2 (semiconductive material) can be investigated via this mode of AFM. It is well known that 2H-MoS_2 (or 2H-WS_2) nanosheet has a semiconductive nature, while 1T-MoS_2 (or 1T-WS_2) is semi-metal. Thus, conductive AFM mode can be used to detect these two different crystal structures of MoS_2 and WS_2 nanosheets. The magnetic properties of the surface and interfaces can also be investigated using a magnetic sensitive tip[27]. Another important application of AFM technique is thickness (t_{FL}) determination of ultrathin 2D nanosheets when these planes are placed on atomically smooth substrates (usually SiO_2/Si and mica substrates)[28-30]. The t_{FL} can be found via a height line profile obtained by AFM data. Knowing the thickness of a "single-layer" of the 2D material (t_{SL}), the number of ultrathin 2D nanosheets (N) can be determined by $N=t_{FL}/t_{SL}$. For example, the AFM images of 2H-MoS_2 nanosheets with different thicknesses of t_{FL}=0.8, 1.5, 2.1 and 2.9 nm have been shown in Figure S2 (h-k). It is well known that the average height of 2H-MoS_2 single layer obtained via AFM technique is about 0.7 nm ($t_{SL}\approx$0.7 nm)[31]. Hence the layer number of MoS_2 nanosheets were determined to be N= 1, 2, 3 and 4, respectively, which have been demonstrated in corresponding optical microscope images Figure S2 (l-o))[31].

2.1.4 X-ray diffraction

The crystalline phase and chemical structure of nanomaterials, particularly 2D nanostructures, can be analyzed using the X-ray diffraction(XRD) patterns due to three main reasons including: i) indicating the presence of pure material with desired crystalline structure in the starting layers bulk precursor [32], ii) confirming the formation of nanosheets especially in exfoliation based synthesis approach [33], and iii) revealing chemical state of the single/few layer products via d spacing calculations[34]. For example, the fabricated graphitic carbon nitride nanosheets via exfoliation method and the correspondence XRD results have been presented in Figure S3a. For layered g-C_3N_4 , the strong XRD peak (002) located at 27.7° is attributed to graphitic materials and is the characteristic of the interlayer stacking reflection of conjugated aromatic systems[35]. A significant reduction in the intensity of this peak indicates the formation of the g-C_3N_4 nanosheet after exfoliation process. Similar results were reported in another work[35] based on two characteristic peaks of the g-C_3N_4 located at 13.6° and 27.4° for (1 0 0) (0.681 nm interlayer spacing derived from the enplaned repeated units) and (0 0 2) reflections (0.326 nm interlayer spacing related to stacking of the conjugated aromatic systems in layered structure), respectively. Moreover on the basis of XRD pattern of prepared graphite oxide (GO) nanosheets exhibited in Figure S3b the (0 0 1) crystal plane of GO with a spacing of 8.33 A$^\circ$, larger than that of graphite, is clear as a finger print of GO. This increment in the spacing distance clearly shows the introduction of a number of oxygen-containing groups on the edge of each layer confirming formation of graphene oxide. The hydrothermal

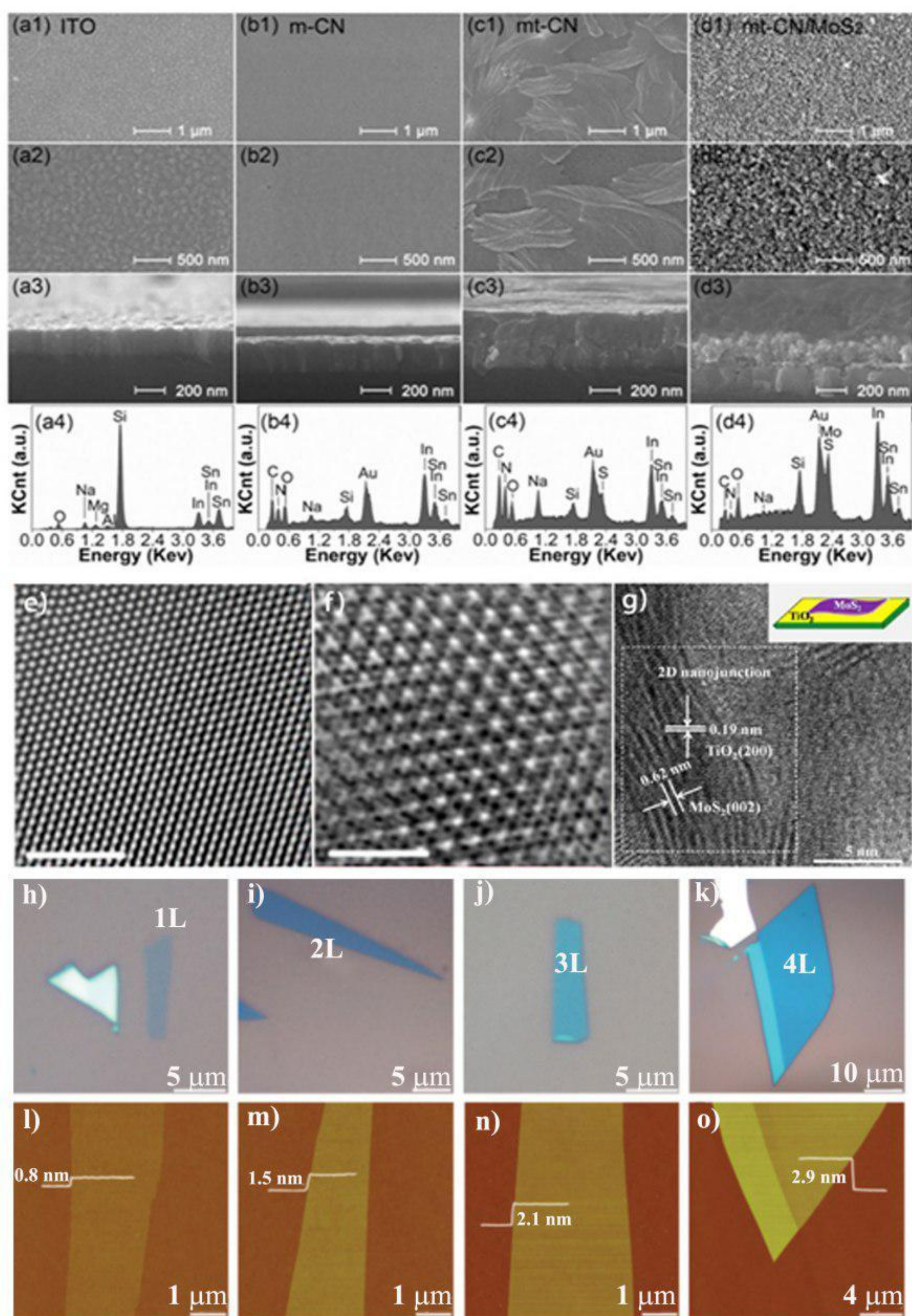

Figure S2.SEM images and EDS spectra of the samples: The low-resolution top view (a1−d1), high-resolution top view (a2−d2), cross-section morphologies (a3−d3) and the EDS spectra (a4−d4) of ITO, m-CN, mt-CN, and mt-CN/MoS_2 thin layers, respectively[21]. (e) HRTEM images of 2H-MoS_2 monolayer before lithiation and (f) 1T-MoS_2 after Li intercalation. Reprinted with permission from. Ref. [23]. Copyright 2014 American Chemical Society (g) HRTEM image of the MoS_2/TiO_2 2D-2D interface heterojunction, The inset is a schematic diagram of the MoS_2/TiO_2 2D-2D heterojunction. Intimate 2D nano-junction between TiO_2 and MoS_2 is clearly observed in the HRTEM images. Reprinted with permission from Ref.[25] . Copyright 2015 American Chemical Society. (h-k) optical microscope images and (l-o) corresponding AFM images of 2H-MoS_2 nanosheets with different thickness. Reprinted with permission from [31] Copyright 2011 Wiely.

treatment of GO resulted in decreasing of the spacing distance to 3.70 A˚, still slightly higher than that of graphite, suggesting the presence of some remaining oxygen functional groups in the prepared graphene (Figure S3b)[36].

2.1.5 Raman Spectroscopy

Raman technique is a spectroscopic method in which vibrational, rotational, and other low-frequency modes in a system can be observed. The energies of vibrational and rotational states and therefore the feature of Raman spectrum, specifically depend on arrangement of atoms in the molecule or material crystal as well as any environmental effect that may change these properties. As a result, the change in positions and intensities of Raman peaks provide very useful structural fingerprint information about chemical and physical properties of the scattering material. For example, in 3D graphite, there is a phonon energy dispersion perpendicular to the graphene planes (along the c direction), whereas for few layer graphene there are finite number of graphene planes. Therefore, several of the in-plane branches of phonon modes are split in the c direction. Particularly, the phonon branches of monolayer graphene split into two branches in bilayer graphene, which correspond to the in-phase (symmetric) or out-of-phase (anti-symmetric) vibrations of the atoms in the two different layers[37] As it is clear, the vibrational modes are different in graphite and graphene with different number of layers. Therefore, their Raman spectra are distinguished from each other and the number of graphene layer can determined by means of its Raman spectrum. In addition, the so-called D band of graphene Raman spectrum represents the disorder and defect-induced Raman band. Also this band can be useful to distinguish between zigzag and armchair edges. The so-called G band reflects the phenomenon of charge transfer (especially at the interfaces) or doping by both electrons and holes and can be interpreted through the change in the position and line width of G-band. The G band shape also represents the strain applied on graphene sheets. The crystalline or turbostratic stacking order can also be distinguished from the shape of the 2D band (also called G′ band) and many other information (the effect of substrate and superstrate interaction, heating and …) can be extracted from Raman spectrum of graphene [38].

Figure S3 (c) and (d) show the changes of graphene nanosheets Raman spectra by superstrate interaction effect and varying the thickness, respectively As it can be seen, two D and D' bands, known as defect-induced bands, have been appeared in Raman spectrum after deposition of 5 nm SiO_2 layer (Figure S3c), indicating that many defects were introduced into the graphene after deposition[39]. Figure S3d indicates that D and 2D band clearly shift to higher wavenumbers by increasing the graphene thickness. The D band intensity decreases by increasing layer numbers and disappears for bulk graphite, but the G band behavior is vice versa. All of these Raman-obtained characteristics information are very useful to deeply investigate 2D graphene nanosheets. As well as graphene, some chemical and physical fingerprint information can be obtained by exploring the Raman spectra of other 2D materials such as TMDs and g-C_3N_4 and etc. Some phonon modes could be activated or quenched when these 2D materials undergo some crystal and structural changes when some interfacial phenomena occur at their atomic contacts with other materials [38]. For example, Figure S3e presents obvious difference between Raman spectrum of 1H-MoS_2 (semiconducting MoS_2 single layer) and 1T-MoS_2 monolayer

[40].Therefore, Raman spectroscopy can be used to recognize the MoS_2 crystal structure. More importantly, the thicknesses of the MoS_2 nanosheets affect the intensities, frequencies and widths of the out-of-plane atomic displacement Raman peak (so-called A_{1g}), therefore these Raman peaks can be used as a "thickness indicator" [41]. The evaluation of this peak and its difference with in-plane mode (E^1_{2g}) as function of MoS_2 layer number has been presented in Figure S3f. As it is clear, this typical characteristic plots can be used to determine the MoS_2 layer number [41].

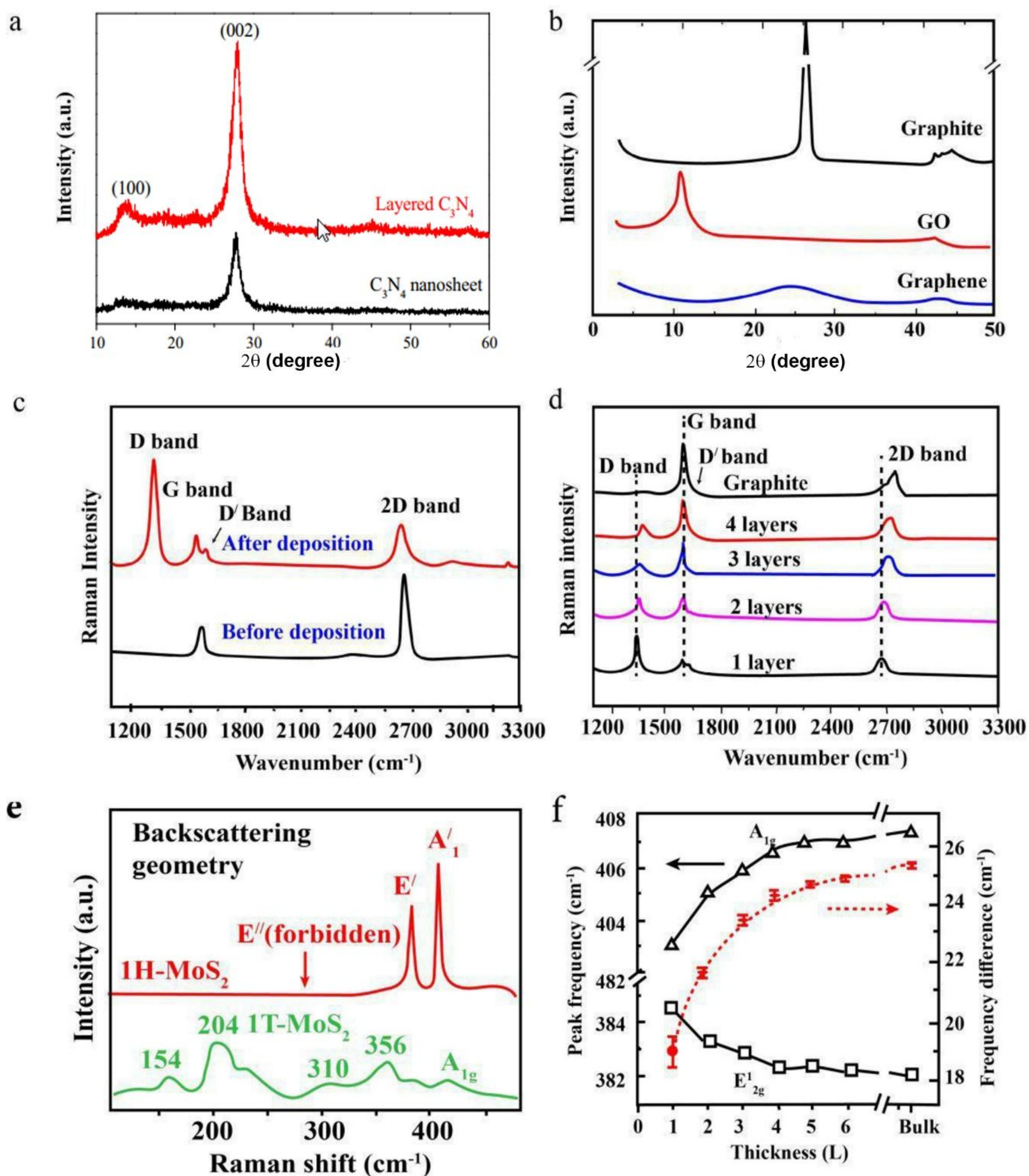

Figure S3: XRD patterns of (a) layered g-C_3N_4 in comparison with g-C_3N_4 structure after exfoliation. Reprinted with permission from [35] Copyright 2014 Elsevier, (b) XRD patterns graphite, graphene oxide derived from modified Hummers method. Reprinted with permission from [36] Copyright 2008 Elsevier. (c) Monitoring the effect of superstrate interaction via Raman spectra of graphene monolayer before and after deposition of the 5 nm SiO_2. (d)Thickness dependence of graphene Raman spectra to determine layer number of graphene sheets. Reprinted with permission from [39] Copyright 2008 Springer. (e) Difference between Raman spectrum of 1H-MoS_2 (semiconducting MoS_2 single layer) and 1T-MoS_2 monolayer. Adapted with permission from [40] Copyright 2014 Macmillan Publishers Limited.. (f) Dependence of E^1_{2g} and A1g Raman modes and their difference to MoS_2 layer number. Reprinted with permission from [41] Copyright 2010 American chemical society.

2.2 Optical/Electrical diagnosis

2.2.1 Ultra violet photoelectron spectroscopy (UPS)

To understand possible mechanisms underlying photocatalytic reactions, the knowledge of conduction and valence band positions of semiconductors with respect to the H^+/H_2 reduction potential and O_2/H_2O oxidation potential is essential. In this regard, photoemission spectroscopy, particularly ultraviolet photoelectron spectroscopy (UPS), has been extensively utilized to determine the band alignment of various structures including the combination of 2D materials with different semiconductors. Considering UPS analysis, practical information on valence bands, which are regarded as the highest filled electronic states with binding energies of ~ 15 eV below the Fermi level, can be acquired. In addition to valence band, surface potentials, chemical interactions at interfaces, and work functions can be determined using UPS analysis[42].

To measure the binding energy of solids in UPS, the Fermi energy of the spectrometer is contemplated as the binding energy reference (E_b= 0). The reference energy can be determined using a clean metallic sample, such as Au, Cu, or Ag. The variation of Fermi level inside the gap with respect to the occupied states in semiconductor-based structures is stemmed from one of the following effects: i) change in electrostatic potential at the surface, ii) different doping of a material, and iii) band bending at the interface. This shift results in a parallel change of all binding energy values including all valence, core, and Auger levels of the sample. It is worth mentioning that a change of the Fermi level shifts not only binding energies of all levels but also the work function of the sample as defined in the following expression [43]:

$$\Delta\phi = \Delta E_f + e\Delta x = eV_b + e\Delta\chi \qquad \text{(S7)}$$

where $\Delta\chi$ is the surface dipole, and V_b is the valence band maximum, which can be determined by using the intersection of the extrapolation of the leading edge of the valence band emission with the background level (Figure S4a) [8]. According to Figure S4b, a typical UPS spectrum consists of three regions including: i) electrons residing at lower energy states represented by a region with low kinetic energy; ii) electrons in the highest levels of the valence band delineated by a peak; and iii) the Fermi-level [44, 45]. Since it is essential to apprehend the band alignment of different structures used in a PEC cell, especially a combination of a 2D material with a large band gap semiconductor, the optical band gap is added to the valence band position so as to obtain the conduction band position. To calculate the optical band gap, the following expression, known as Tauc's equation, can be constructed from optical absorption data (Figure S4c)[45] ,

$$\alpha h\nu = A(h\nu - E_g)^n \qquad \text{(S8)}$$

where A is a constant depending on the nature of conduction band and valance band, hν is incident photon energy, and E_g is the band gap energy. Also the value of the exponent, n, depends on whether the transition of a sample is direct or indirect.

2.2.2 Photoluminescence spectroscopy

It is well established when a semiconductor material with band gap energy (E_g) is irradiated by photon with energy of hν, and its energy is greater than hν ($h\nu \geq E_g$), an electron is excited from the valance band (VB) to the conduction band (CB) and a positive hole is remained in the VB. The generated electron-hole pair can undergo various processes. The emission spectrum (photoluminescence spectrum, PL) obtained from radiative relaxations provides very useful information from both qualitative and quantitative viewpoints. Most important processes leading to various phenomena are illustrated in (Figure S4d). Several relaxation processes can occur and provide different characteristic features in PL spectrum. Therefore, PL spectrum can be interpreted to give useful information about electronic levels of excited semiconductor including donor and acceptor levels, Excitonic energy levels, surfaces and interface trap states and so on [46].

Recombination of electron-hole pairs generated by light absorption is not in favor of photochemical reactions. Hindering this recombination process, which can be caused by electron-hole separation at the interfaces of two semiconductors, is desired and will increase the efficiency reactions. Increase in electron-hole lifetime by preventing their recombination can be analyzed both qualitatively and quantitatively by photoluminescence (PL) spectroscopy. Preventing electron-hole recombination at the interface of the materials will result in PL intensity quenching. The more the PL quenching is observed, the better electron-hole separation is occurred. Therefore, in addition to peak positions information in PL spectrum, the quenching or rising of PL peak intensity also shed light on electron-hole life-time and undergoing interfacial processes Figure S4e). If N_0 defines the number of generated electron-hole pairs by light absorption at t=0, the population of these excited states after time t, N(t), can be obtained as $N(t) = N_0 e^{-t/\tau}$ where τ represents electron-hole life time [47]. In order to determine the value of τ, two conditions should be full filled: i) the PL peak intensity should be recorded as function of "t" immediately after excitation, and ii) t should be substituted by τ which leads to PL intensity reduction by 1/e of its initial value. Longer life-time (bigger τ) means that the electron and hole have more time to participate in photocatalytic (PC) reactions before their recombination and thus leading to higher PC and PEC yield (Figure S4f) [48].

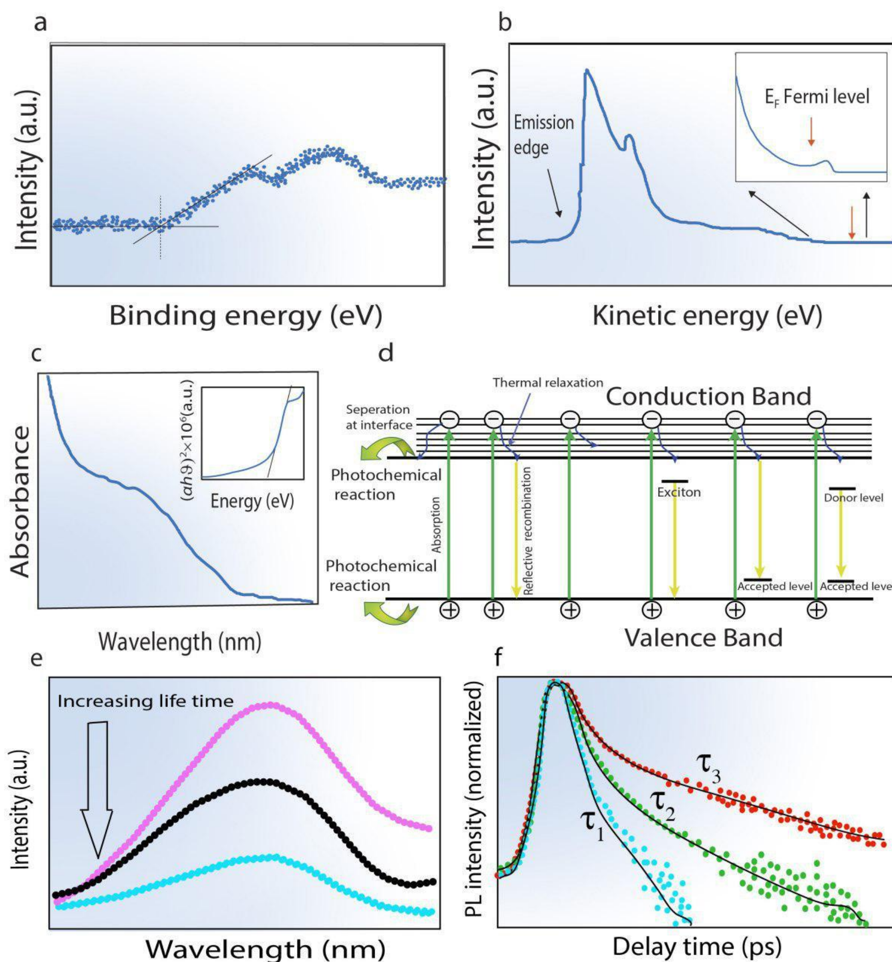

Figure S4: (a) Determination of Fermi-level. Adapted with permission from Ref. [8]. Copyright 2012 The Royal Society of Chemistry. (b) The VB UPS spectra[42]; (c) UV/Vis absorption spectrum inset: Tauc plot for bandgap calculation. Adapted with permission from Ref. [45]. Copyright 2015 Wiley-VCH. (d) Various possible processes for electron-hole pairs generated by light absorption in a semiconductor, (e) typical photoluminescence spectra of a semiconductor with different PL intensities. Lower PL intensity, means longer e^--h^+ life time Adapted with permission from. Ref [47].Copyright 2014 Elsevier.(f) Typical time resolved PL spectra with different electron-hole life time ($\tau_3>\tau_2>\tau_1$) Adapted with permission from [48]. Copyright 2007 American Chemical Society.

2.3 Photoelectrochemical investigation

2.3.1 Photoresponse

Photocurrent measurement

Photocurrent measurements are main and powerful methods for studying the properties and performance of photoelectrodes in PEC cell and include photocurrent–voltage (j-V), photocurrent transients (j-t) response and photocurrent “action spectra” or the Incident-Photon-to-Current Efficiency (IPCE). By using different photocurrent measurements, PEC efficiencies and charge carrier transient time of photoanodes or photocathodes for water splitting reaction can be obtained under different conditions.

In general, j-V measurement is carried out by measuring the (photo) current in the dark, under constant irradiation, or by switching the light on and off at a fixed frequency while the potential is swept at a constant scan rate-usually between 1 and 50 mV/s. The following information can be obtained from j-V measurements [1]:

The sign of the photocurrent under illumination: Anodic (positive photocurrent Figure S5a) for n-type semiconductor or cathodic (negative photocurrent (Figure S5b) for p-type semiconductor).

The photocurrent onset potential: The potential that the photocurrent generation begins is called the onset potential. The onset potential can be applied to define the flat band potential of a semiconductor. The flatband potential is the potential at which the conduction and valence bands are flat and no band bending occurs at the semiconductor/electrolyte interface (The most powerful technique for measure the flatband potential is Mott-Schottky analysis that is fully described in section 1.3.2) At potentials positive with respect to the flat band potentials, a depletion layer forms and the separation of the photogenerated electrons and holes produces a photocurrent.

Solar to hydrogen conversion efficiency(STH*):* The energy conversion efficiency can be calculated from the photocurrent density(j_{photo}) by using the following relation [49]:

$$\eta_{STH} = \frac{j_{photo}(V_{redox} - V_{bias})}{P_{light}} \quad \text{(S9)}$$

where P_{light} ,V_{redox} and V_{bias} are the incident light intensity,1.23 V and applied bias voltage, respectively. This expression is named overall solar to hydrogen (STH) efficiency.

The dark current vs. the applied potential: When the dark current starts to increase, the electrochemical oxidation reaction of water at the surface occurs at a potential which is more positive than potential at the starting point.

Effect of both-sided illumination on charge transport: When front-side of a semiconductor is illuminated, most of the light absorption is accumulated at the semiconductor/electrolyte interface. In this case, the photogenerated electrons have to pass a larger distance before reaching the interface than the photogenerated holes. On the other hand, the situation is reversed for backside irradiation (Figure S5c).

Transient time constant prediction: When the light is switched on and off with a shutter, distinction between the dark current and the photocurrent can be easily detected and lead to accurately define the photocurrent onset potential. By turning light on, the transient is obtained and such transients show recombination of the electron-hole pairs. In this case, the photocurrent rapidly rises to its peak value (j_0) and then because of recombination of the photogenerated electrons and holes (j_0-j_{SS}), it falls off to a steady-state value (j_{SS}) (Figure S5d).The recombination occurred as a result of two possible processes: accumulation of electrons in the bulk

and accumulation of holes near the surface, and/or trapping of electrons or holes at surface states [1]. The kinetics of recombination process is controlled by the following equation [50]:

$$D = e^{(-\frac{t}{\tau})} \qquad \text{(S10)}$$

where D is defined as

$$D = \frac{(J_t - J_{SS})}{(J_0 - J_{SS})} \qquad \text{(S11)}$$

where t, τ and J_t denote interaction time, transient time constant and photocurrent at time t , respectively. The slope of lnD vs. time plot determines the transient time constant. Thus, lower slope represents a longer transient time constant.

<u>Wavelength-Dependent photocurrent (action spectra):</u> The spectral response of a photoelectrode can be investigated by recording the photocurrent as a function of the wavelength at a constant applied potential. Due to some degree of current drift over a time scale of 5–10 min, photocurrent are measured by chopping the light on and off. Furthermore, by utilizing a calibrated photodiode, the intensity of the incoming light can be monitored as a function of incident light wavelength in a separate measurement. By using this technique, the following information can be attained [1].

***<u>IPCE efficiency</u>*:** The IPCE is one of the most essential diagnostic measurements to evaluate the PEC performance of a photoelectrode. It measures the amount of the collected photogenerated electrons at the back contact of the photoanode per incident photon as a function of wavelength (λ) illuminated on surface (Figure S5e).

Quantum efficiency as a function of wavelength is a particularly useful parameter for understanding IPCE[51] . The definition of the external quantum efficiency is the fraction of the incident photons that is converted to electrons that can be measured by the outer circuit. In addition, the optical absorption of the photoelectrode, the width of the space charge layer (section 3), and the minority carrier diffusion length are the most crucial parameters that influence the amount of IPCE for any photosystem. By using a standard three-electrode configuration, the IPCE of a desirable semiconductor photoelectrode at wavelength λ is described as following [5, 9]:

$$IPCE(\lambda) = \frac{hc}{e}\left(\frac{j_{photo}(\lambda)}{\lambda P(\lambda)}\right) \qquad \text{(S12)}$$

where P(λ) is the light intensity (mW/cm^2) at a specific wavelength, j_{photo} (λ) is the photocurrent density (mA/cm^2), h is the Planck's constant, c is the speed of light and e is fundamental electric charge. It is worth

mention that, in addition to the optical spectroscopy techniques, measuring IPCE is also useful to calculate the band gap energy. However, the estimated band gap energy obtaining from IPCE may be higher due to the onset of photocurrent, which is limited by slow kinetics, and electron transport [52] .

Additional important optical quantity is the APCE, or absorbed photon-to-current conversion efficiency (internal quantum efficiency). It corrects for reflection losses and is expressed by the following relation [1]:

$$APCE(\lambda) = \frac{IPCE(\lambda)}{A(\lambda)} = \frac{IPCE(\lambda)}{1 - R - T} \quad \text{(S13)}$$

in here A, R and T are absorption, reflectance and transmittance at wavelength λ, respectively. By using the IPCE values measured under monochromatic irradiation (at a specific λ), the photocurrent under actual solar (AM1.5) irradiation can be predicted as follows:

$$J_{solar} = \int (IPCE(\lambda) \times \varphi(\lambda) \times e) d\lambda \quad \text{(S14)}$$

where, J_{solar} ,φ(λ) and e are the total solar photocurrent (A/m^2), the photon flux of sunlight ($photons/m^2/s$) and the elementary charge (C), respectively. φ(λ) can be calculated from tabulated solar irradiance data, E(λ),using the following expression:

$$\varphi(\lambda) = E(\lambda) / (hc / \lambda) \quad \text{(S15)}$$

Despite some overlap between the information from j-V measurements and photocurrent action spectra (IPCE), the action spectra are generally recorded at much lower light intensities with a relatively small photocurrents under illumination and the dark condition; hence, dark current may no longer be negligible. Therefore, the photocurrent always is reported as the difference between the current under illumination and the dark condition [1].

Open-circuit potential (OCP) decay measurement: The open-circuit potential (OCP) decay analysis is another powerful tool to study electron life time or recombination rate constant. This technique measures photovoltage versus time without an external applied bias voltage during illumination interruption. Figure S5f shows the decay profiles of photovolatge (V_{OC}) after light was turned off. Main advantages of this method over frequency or steady-state-based methods include: i) simple method, ii) calculation of lifetime as a function of open V_{oc} at high-voltage resolution, and iii) the data treatment is simple for obtaining the main information from the recombination mechanisms. By using the following equation, the life time of photogenerated electrons can be calculated in each energy state [53]:

$$\tau_n = -\frac{kT}{e} \left(dV_{oc} / dt \right)^{-1} \quad \text{(S16)}$$

where, t, e, τ_n and kT are time, elementary charge, lifetime in the dark condition and thermal energy, time, respectively.

In other data analysis, the OCP curve is normalized and the data is fitted to a first-order kinetic model for obtaining an average recombination rate constant [54]:

$$\frac{V - V_{ph}}{V_0 - V_{ph}} = 1 - \exp(-k_r t) \qquad \text{(S17)}$$

in here, V, V_0, V_{ph} and k_r are the OCP (at any time), V_0 is the stationary OCP value in the dark, V_{ph} is the photostationary OCP value, and k_r is the pseudo-first order recombination rate constant. The open circuit decay kinetics can determine the charge recombination rate in the photoelectrode.

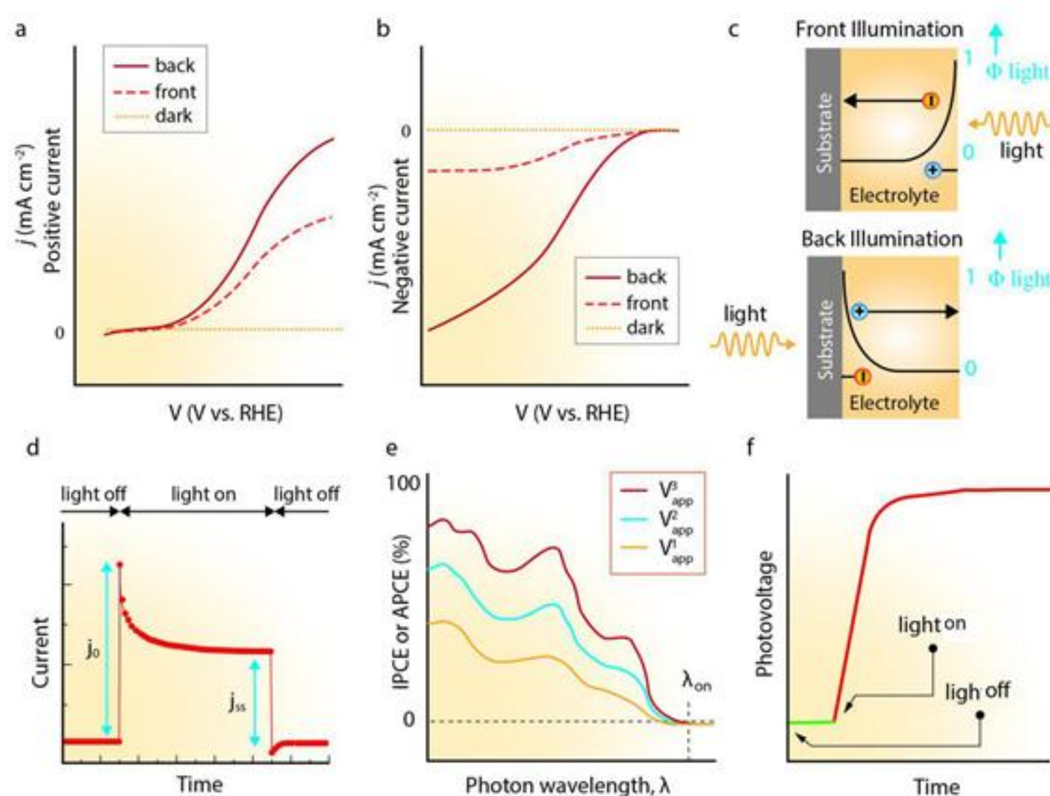

Figure S5: current–voltage curve under front- or back-side illumination and in the dark condition for (a) photoanode and (b) photocathode. (c)The difference between front- and back-side illuminations of a photoelectrode. The curved line shows the exponentially decaying light intensity in the film (Beer –Lambert law). Adapted with permission from Ref.[43]. (d) Typical photocurrent transient response curve at a constant potential. Adapted with permission from Ref.[1]. (e) The incident photon-to-current conversion efficiency (IPCE) or absorbed photon-to-current conversion efficiency (APCE) with different constant applied potential (E^{i}_{app}). Adapted with permission from [55] (f) the open-circuit potential (OCP) decay versus time after light is shut down Adapted with permission from Ref. [56]

2.3.2 Impedance and Mott–Schottky Analysis

Electrochemical impedance spectroscopy (EIS) analysis is employed to measure the kinetics of charge transfer which limits the efficiency of the PEC water splitting[57]. Despite the fact that EIS is quite simple technique, the interpretation of the results is mostly complex and needs to apply appropriate models. The impedance analysis used in solar water splitting research includes frequency scan which determines the charge transfer resistance of interfaces and potential scan determines donor density and flatband potential (Mott–Schottky plot) of a photoelectrode. The fundamental principles of all these measurements are discussed below:

Frequency scan

The goal of frequency-based techniques is to find information about the internal charge transfer and storage process in the semiconductor electrodes with the intention to understand about the mechanism of the reaction involved. In Frequency techniques, like EIS, a small perturbation in specified steady state variable of the system, like voltage, or light intensity, leads to output signals forming an impedance spectra with high resolution of kinetic processes in a wide range of frequencies. Essentially, EIS consists of the measurement of an alternative current (AC) at a certain angular frequency ω when an AC voltage is applied to the system$\widehat{V}(\omega)$. Then the impedance (Z) at frequency ω is characterized by the following expression:

$$Z(\omega) = |z| \exp(i\varphi) = \frac{\hat{V}(\omega)}{\hat{I}(\omega)} \quad \text{(S18)}$$

$$\mathrm{Re}\,al(Z) + \mathrm{Im}\,aginary(Z) = Z' + iZ'' \quad \text{(S19)}$$

where ϕ represents phase difference between voltage and current and ω is angular frequency. The plot of Z'' as a function of Z' called: "Nyquist plot" and plot of ϕ vs log ω named "Bode plot". Examples of these plots will be discussed in Figure S6a and b.

Impedance spectroscopy provides the possibility to evaluate the charge transfer in semiconductor photocatalysts by the utilization of complex physical approach such as a transmission line model [43]. The EIS measurements of the PEC water splitting could be conducted in both dark and illumination. The most common equivalent circuits used to fit the EIS data is "Randles" circuit which consists of three parts including: (i) the electrolyte solution resistance (R_s); (ii) the interfacial charge transfer resistance across the electrode/electrolyte (R_{ct}) and (iii) the constant phase element (CPE) for the electrode as shown in Figure S6c [33].

The most important information that can be extracted from EIS data in metal oxide semiconductor/electrolyte systems can be listed as following:

1- The nature of Nyquist plot (Figure S6a) obtained in the dark condition is a semicircle representing the charge transfer resistances in the total frequency range. Moreover, charge transfer resistance under illumination is considerably less than in dark conditions.
2- The Bode plots exhibit (Figure S6b) only one constant time indicating the overlapped impedance response of the semiconductor electrode and the electrolyte solution.
3- The interface structure of semiconductor electrode/electrolyte divided into the depletion and the Helmholtz layers, is investigated in both dark and illuminated conditions. In dark condition, the semicircles assigned to

the depletion and the Helmholtz layers are overlapped and as a result only one peak is observed in the diagram (Figure S6a)

4- In the Nyquist plot under sun simulated conditions, two distinguished semicircles can be observed. A small semicircle in the high frequency range, attributed to the charge-transfer phenomena in the depletion layer of semiconductor; and the low-frequencies arc, ascribed to kinetics of the electron transfer at the Helmholtz layer which is shown in the inset of Figure S6a.

5- The similar results may be also concluded from the Bode plots (Figure S6b). The peak in right side of the Bode-phase diagram related to the depletion layer with higher transient time, while the peak appeared in left side attributed to the resistance at the Helmholtz layer with lower transient time.

Potential scan

When an n-type semiconductor and electrolyte are brought into contact, where Fermi level of the semiconductor is higher in energy compared to redox Fermi level ($E_{F(redox)}$) of electrolyte (Figure S6d), the electrons transfer from the semiconductor to the redox Fermi level of electrolyte, hence their Fermi levels become equal (Figure S6e)[1, 58]. After this equilibrium, the semiconductor is charged positively (forming space charge region) with carrier densities much lower than those in electrolyte solution and thus band bending occurs at the surface of semiconductor in space charge region. By varying the applied voltage to the semiconductor, the $E_{F(redox)}$ and E_F of the semiconductor levels are spreading apart. At a potential called flatband potential, V_{fb}, band bending or space charge region is disappeared (Figure S6f). Determination of the flatband potential can be conducted by several techniques. One of the conventional and useful methods is Mott–Schottky analysis. By using charge density and potential difference in space charge region of the semiconductor and placing these two parameters into Poisson's equation, then by solving it leads to Mott–Schottky equation described below [1]:

$$\frac{1}{C^2} = \frac{2}{e\varepsilon\varepsilon_0 A^2 N_D}(V - V_{fb} - \frac{k_B T}{e}) \tag{S20}$$

where C, A, N_D, V, k_B , T, ε, ε_0 and e are the space charge capacitance, area of electrode, donor density, the applied voltage, Boltzmann's constant, the absolute temperature, the dielectric constant of the semiconductor in use, the vacuum permittivity (8.85×10^{-12} C^2/Nm^2) and elementary charge (1.6×10^{-19} C), respectively. Flatband potential is determined by interception of straight section of $1/C^2$-V plot on V axis while donor density can be obtained from the slope of this section, respectively(Figure S6g) [58]. The Mott-Schottky equation can be used for both n- and p-type semiconductors. The majority carriers in n-type semiconductor are electrons and the Mott-Schottky plot has a positive slope, whereas for the p-type semiconductor, the slope of the plot is negative with holes as majority carriers [1].

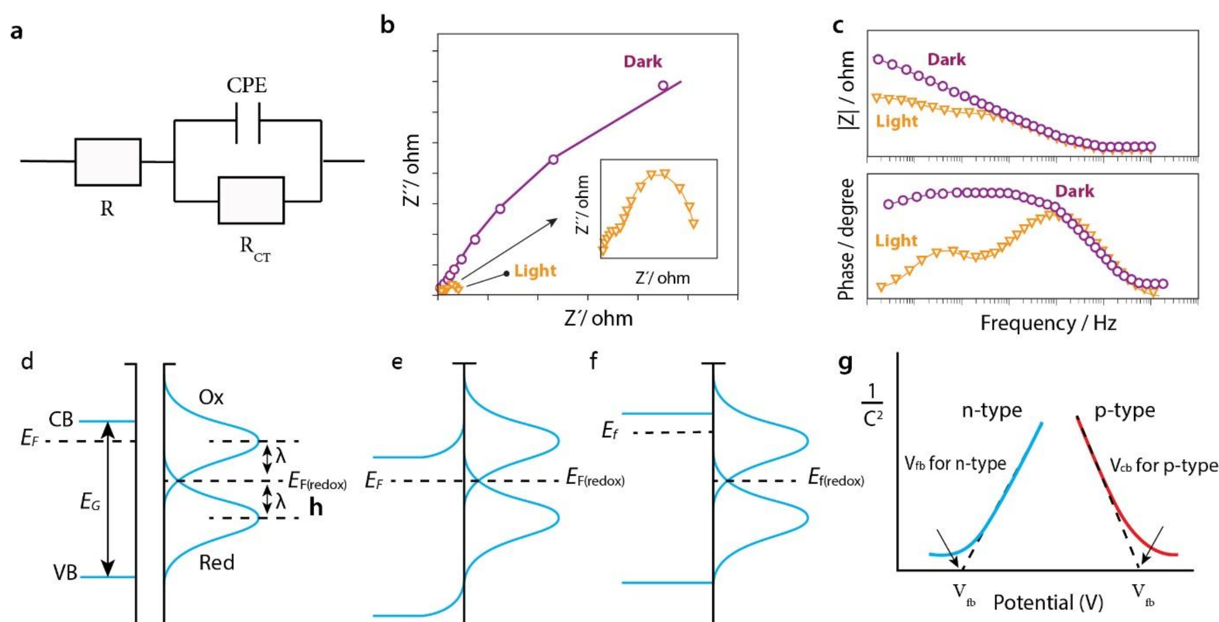

Figure S6 (a) Simplified Randles model. Reproduced with permission from. Ref. [43]. Copyright 2016 Springer (b) Nyquist diagram and (c) Bode plots obtained in the dark and under simulated sunlight at applied bias potential in a three-electrode configuration semiconductor in a 3-electrode configuration Adapted with permission from. Ref. [33]. Copyright 2016 Elsevier. (d) The valence band (VB), conduction bands (CB), Fermi level (EF), band-gap energy (EG) for n-type semiconductor and the oxidation (Ox) and reduction (Red) states in electrolyte solution with their corresponding Fermi level (EF(redox)) and solvent-reorganization energy (λ). (e) Band bending and equilibrium between the n-type semiconductor and electrolyte (f) Semiconductor-electrolyte interface situation by applying flatband potential. Reproduced with permission from. Ref [52, 59]. (g) The $1/C^2$ vs V plot for n and p-type semiconductor [1].

2.4 Theoretical insight

Even though extensive experimental studies offer valuable information on 2D/semiconductor interfaces and mechanism of water splitting at these heterojunction, there is still deficiency of fundamental understanding about the impact of interfacial structure and electronic properties of 2D/semiconductor junction. In general, the PEC and PC activities of 2D/semiconductors are defined by their electronic and interface structures such as stacking orders, displacement, interfacial atomic composition, and arrangement of boundaries.

The wave functions of the atoms involved in interface manage whether to form chemical bonds or physical adsorption. The relative locations of the electronic bands existing at both sides of the interface have great impact on the PEC activity, as they determine the optical properties and charge transfer direction[60]. Thus understanding of the relation between interface structure and the electronic properties can play a fundamental role in designing of the high performance composite photocatalyst. In order to support any experimental result, extensive theoretical investigations must be conducted to elucidate the role of 2D material interfaced semiconductor metal oxides on several important issues including band gap energy, surface tendency to chemical bond formation, charge transfer through interface, and activity under visible. Fortunately, density

functional theory (DFT) calculations can provide a great opportunity to extend our knowledge to understand the relationship between the interface configuration, electronic and optical properties at atomic-scale resolution in PC and PEC reactions. Generally, in studying a photoactive material, like semiconductors, three essential steps and their related parameters should be considered as following:[61]

2.4.1 Optical absorption spectra:

Step 1: The light absorption, it leads to excitation of an electron from the valence band to the conduction band of the SC, resulting in generation of electronic vacancy, a hole (h^+), in the valence band. The electron-hole interaction, known as an exciton, is Coulombic in nature. For water splitting, the optimum band gap must be around 2 eV[1]. Thus, optical absorption spectra, the electronic band structure and band alignments should be determined in order to evaluate photoresponce of the SC under investigation. This step is shown in Figure S7a.

The calculation of excitation energies provides information on the location of visible and near-visible UV absorption peaks in the spectrum. The peak intensities are estimated by calculating transition dipole moments between the states involved in the given excitation. Time-Dependent DFT method (TD-DFT) is the most common way of calculating other properties such as the excitation energies, optical absorption and emission, polarizabilities, and higher order nonlinear effects. The stronger optical absorption leads to a higher efficient PEC/PC system. The optical absorption coefficient $\eta(\omega)$ is related to the frequency-dependent dielectric matrix described as below[62].

$$\varepsilon_2(\hbar\omega) = \frac{2e^2\pi}{\Omega\varepsilon_0} \sum_{k,vc} \left| \left\langle \psi_k^c \middle| u.r \middle| \varphi_k^v \right\rangle \right|^2 \delta(E_k^c - E_k^v - E) \qquad \text{(S21)}$$

where Ω, ω, u, v, and c are the unit-cell volume, photon frequency, the vector defining the polarization of the incident electric field, valence bands, and conduction bands, respectively. A typical optical absorption spectrum obtained from computational analysis is given in Figure S7b. Further detail on $\eta(\omega)$ calculation can be found elsewhere [63].

2.4.2 Electronic structure calculation

Band Gap Determination

Monoelectronic bandgap: it defines the energy gap (E_g) between the top of the valance band and the bottom of the conduction band acquired by solving self-consistently of the mono-electronic Khon−Sham (KS) equations[64]. The major limitation in solving these equations is that the actual form of the exchange-correlation functional is not known. Different approximation methods like local density approximation (LDA), generalized gradient approximation (GGA) and Heyd-Scuseria-Ernzerhof (HSE06) hybrid functional have

been implemented to estimate the exchange-correlation (XC) function (Figure S7c) [65]. Generally GGA determines band gap of metal oxides semiconductors with a lower estimation whereas HSE06 gives more accurate values for these materials. Moreover, a higher computational cost is needed for the latter.

Band edge positions

The electronic band edges alignment (Figure S7d) is one the vital parameters for judging a material's ability to be utilized in a solar driving water splitting cell[1]. The valence band maximum (VBM) of a material is usually supposed to be identical to the KS VBM in the literature [66]. The conduction band maximum (CBM) can be calculated by adding the KS VBM to an energy gap, however the existence of discontinuity in the XC energy makes this method inaccurate for calculating the VBM of a semiconductor from KS approach. Nevertheless, another theorem also describes that DFT is formally precise for determining the band gap center (BGC), specified here by energy band gap center (EBGC).

The quasiparticle (QP) gap is principally the ionization potential minus the electron affinity of the material. The electron affinity of the material is equivalent to the gap measured by photoemission electron spectroscopy (PES) experiment, therefore, by means of the GW method, along with the obtained BGC, the VBM and CBM can be calculated as follows,[66]

$$E_{VBM} = E_{BGC} - 1/2\ \mathrm{E}_g \qquad \text{(S22)}$$

$$E_{CBM} = E_{BGC} + 1/2\ \mathrm{E}_g \qquad \text{(S23)}$$

E_g, E_{BGC}, E_{VBM} and E_{CBM} are the QP band gap, band gap energy center, valence band maximum and conduction band maximum respectively.

2.4.3 Charge transport analysis

Dielectric constant

Step 2: **Dissociation of excitons**. Following the absorption occurrence described above in step 1, separation of electron and hole results in formation of free charge carriers, which is involved in water oxidation and proton reduction, respectively. The low binding (Figure S7e) energy, E_b, between exciton leads to the enhancement in dissociation rate. The required energy for dissociation could be supplied with thermal energy (k_BT). It means that E_b should be lower than k_BT (around 25 meV at room temperature). The strength of the binding energy depends on the amount of dielectric constant of the semiconductor. The lower E_b is related to better separation between electron-hole which originates from the higher dielectric constant[61].

Effective mass

Step 3: Charge carrier's diffusion the ideal path for free electron and hole is that they diffuse toward the photocatalyst surface sites instead of their recombination (Figure S7f). The diffusion coefficient, D, represents the capability of diffusion of electron and hole in a semiconductor depends on the mobility, μ, of the charge carrier through the Einstein equation (S24), which is related to effective mass (m^*) and the collision time (τ) of the charge carrier (S25).

$$D = \frac{k_B T}{e}\mu \tag{S24}$$

$$\mu = e\frac{\tau}{m^*} \tag{S25}$$

the decreasing in m^*results in increasing of charge carrier diffusion. Figure S7g illustrates the effective mass approximation from the VB and CB of the band structure.

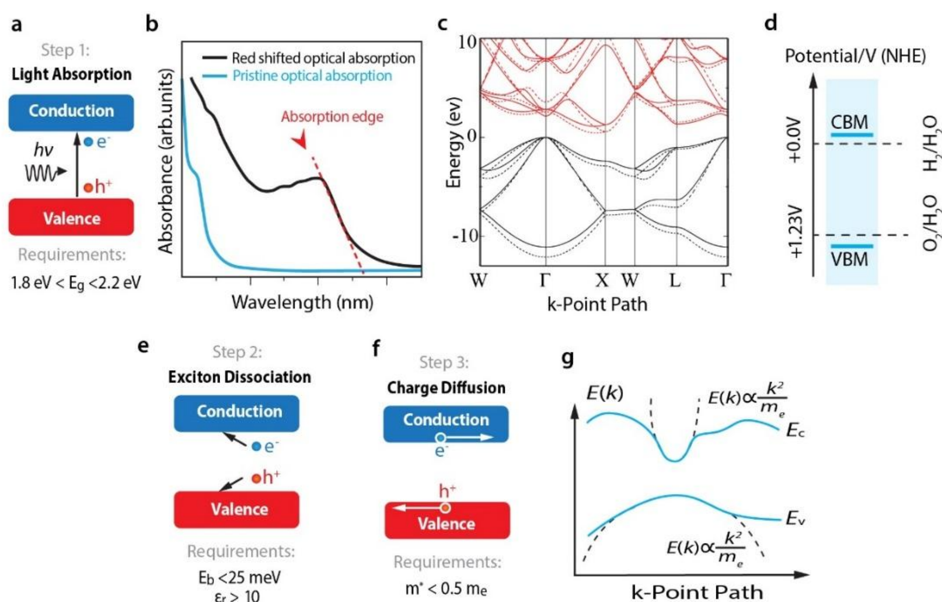

Figure S7 (a) Schematic representation of the first fundamental step encountered in any photochemical system involving a semiconductor. The quantitative values of the requirements are determined for photovoltaic and water splitting applications. Adapted with permission from. Ref. [61]. Copyright 2014 American Chemical Society. Typical (b) Calculated absorption spectra for semiconductor. (c) Calculated band structure for a semiconductor (d) Band edge alignment of suitable semiconductor for PEC/PC water splitting reaction relative to water oxidation and hydrogen reduction potential.[1](e) Second fundamental step encountered in photochemical systems involving a semiconductor (f)Third fundamental step encountered in photochemical systems involving a semiconductor third Adapted with permission from. Ref. [61]. Copyright 2014 American Chemical Society (g) Schematic illustration of the effective mass approximation.

3 2D materials in brief

From historical view point, research on two-dimensional (2D) materials has been initiated since 1859[67]. It is one of the most widely studied research fields due to their novel properties and multipurpose potential applications. Generally, 2D materials are composed of strong covalent bonds lead to in-plane stability of 2D crystals and weak, van-der-Waals-like forces which form a stacked structure. Following discovery of graphene in 2004, a new horizon has been opened to explore other 2D layered materials such as metal chalcogenides, transition metal oxides, graphitic carbon nitride, hexagonal boron nitride and etc. These 2D materials can be integrated with three-dimensional (3D) semiconductor photocatalyst as a new building block to form an efficient light energy harvesting interfacial heterostructure assemblies [68]. photovoltaic devices, hydrogen evolution catalysis, transistors, photodetectors, DNA detection, and lithium ion batteries

3.1 graphene

The discovery of graphene, the first mono layer two dimensional material, by Novoselov and Geim revolutionized material science in early 2000 [69]. The significance of this success was revealed in 2010, when the Nobel Prize was given to both scientists. The honeycomb crystal lattice of graphene is composed of atomically thin layered sp^2 carbons. The structure can be assumed as a triangular lattice with a foundation of two atoms per unit cell (showed in Figure S8a), which could be used to calculate the band structure of single layer graphene using a tight-binding approximation. The crystal energy of graphene lattice is the same as crystal energy of diamond. The band structure of intrinsic graphene represents a zero-gap semiconductor or semi metals (Figure S8b), furthermore the density of states is zero at the Fermi level resulting from the identical environment of the two carbon atoms[70]. Electronic bands close to the six angles of the two-dimensional hexagonal Brillouin zone crossed the Fermi level and, as a result, valence band and conduction band meet at the K and K′ high symmetry points, which identified as Dirac points or charge neutrality regions (Figure S8c) [71-73].

The most remarkable feature of the graphene energy spectrum is that the charge transport can be explained by a Dirac spectrum for massless fermions instead of the standard Schrödinger equation. Since the quasi-particles in graphene are massless relativistic particles formulated by the Dirac equation, they show a linear dispersion relation according to the equation $E = \hbar \upsilon_f |K|$ (in here, instead of speed of light (c), the Fermi velocity ($\upsilon_f \approx c/300$) is used). Consequently, irrespective of their momentum, electrons of graphene travel at a constant velocity ($\sim \upsilon_f$). Owing to the linear dispersion characteristic, the quasi particles in graphene act in different way as compared to metals or semiconductors, thus the energy spectrum of graphene is represented approximately by free electron-like parabolic dispersion relation (Figure S8d). Moreover, graphene is a perfect spin carrier due to the extraordinarily low spin–orbit (SO) interaction [74].

There are different ways to modify the band structure of graphene such as heteroatom doping and electrostatic field tuning, which usually converts semimetal graphene to a small bandgap n-type or p-type semiconductor by detuning away the Fermi level from the Dirac point (Figure S8e). Furthermore, mono-layer graphene exhibits high optical absorption coefficient of 7×10^5 cm^{-1} over a wide range of wavelength from

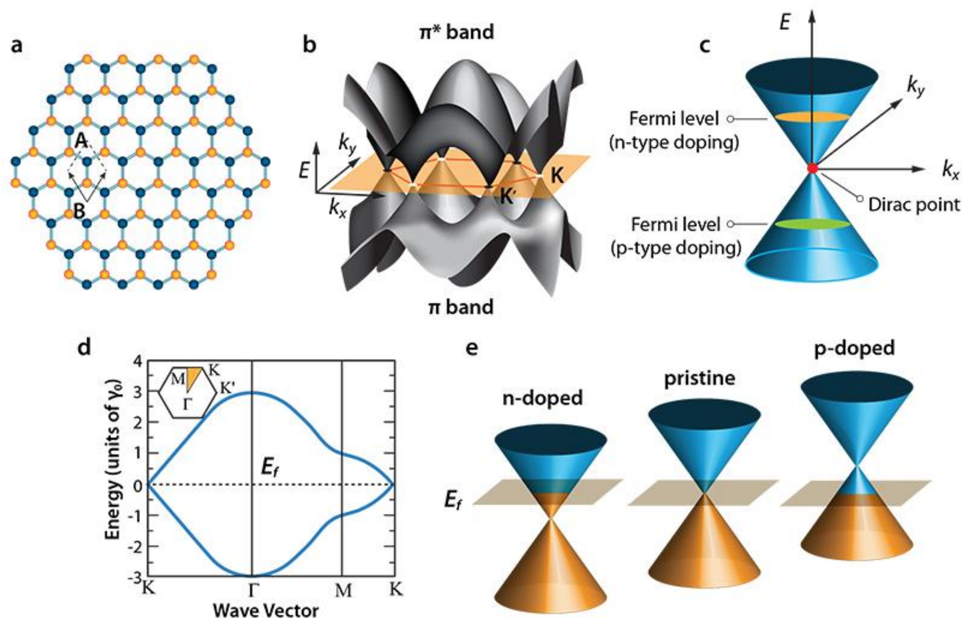

Figure S8(a) Honeycomb hexagonal crystal structure of graphene with two atoms (A and B) per unit cell; (b) three dimensional illustration of the electronic band structure of graphene; (c) approximation of the Dirac points of graphene band structure (d) band structure dispersion of graphene. Reproduced with permission from Ref. [73]. Copyright 2010 American Chemical Society and (e) band structure of mono layer graphene representing p- and n-type doping; with respect to the Fermi level. Reproduced with permission from Ref. [77]. Copyright 2016 The Royal Society of Chemistry.

ultraviolet to visible region, which is much higher than that of conventional semiconductor materials [75]. In addition to its unique optical properties, high Young's modulus (up to ∼1 TPa for defect-free graphene) and high thermal conductivity (up to ∼5000 W/mK for suspended single-layer graphene at room temperature), it makes graphene as a suitable candidate to be utilized in different devices like light-emitting diodes, transistors, solar cells, photocatalysts, biosensors, photodetectors, and lithium ion batteries [74].

Aside from the mentioned modification routes, the chemical functionalization of graphene is an alternative method to modify its electronic properties[76]. For instance, oxygen functional groups (electron accepting functional) or nitrogen functional groups (electron-donating functional) turn graphene into a p- or n-type semiconductor, respectively. Accordingly, functionalized graphene can be considered as a promising candidate of non-metal semiconductor photocatalysts. In this regard, graphene oxide (GO), which is usually obtained by chemical exfoliation of graphite over severe oxidization, extensively used as an single layer graphene decorated with different oxygen- functional groups (such as hydroxyl, epoxy, and carboxyl) on both the basal

plane and the edge. Due to the presence of sp^3 hybridized carbon atoms in GO which disrupt the delocalized π -conjugation in graphene, makes it an insulator in contrast to the quasi-metallic pristine graphene.[75]

3.2 Transition metal dichalcogenides

The transition metal dichalcogenides (TMDs) (e.g., MoS_2, WS_2, and $TiSe_2$) , as seen in Figure S9a, are large group of layered materials with the generalized formula MX_2, where M is a transition metal element from group IV (Ti, Zr or Hf), group V (V, Nb or Ta) or group VI (Mo, W), and X is a chalgogen atom (S,Se,Te)[78, 79].

Bulk TMDs (X-M-X) composed of three atomic layers in which the M is hexagonally packed between two X atoms where M and X are bonded covalently. However, adjacent layers of MX_2, are connected by weak van der Waals bonding, to form bulk crystals. These van der Waals forces make crystal readily cleave along the layer surface (Figure S9b).

Bulk TMDs can be exfoliated into single or few layered structures by physical or chemical routes, such as adhesive tape exfoliation, solvent-assisted exfoliation, and chemical exfoliation via lithium intercalation[80]. In comparison to bulk structures, monolayer and few-layered TMDs demonstrate various appealing characteristics due to their quantum confinement and surface effects. For instance, a transition from indirect optical band gap to direct optical band gap takes place when a bulk semiconducting trigonal prismatic TMD is exfoliated to mono layer TMD, which leads to enhanced photoluminescence (PL).The four electrons of metal (M) with the oxidation states of +4 fill the bonding state of a TMD. The d-orbital, filled from d^0 to d^6, affects the metal coordination which results in the emergence of size dependent exciting electronic properties. In this context, d^0 semimetals (TiX_2), d^1 (NbX_2 and TaX_2), or d^3 (ReS_2) exhibit metallic properties, while d^2 semimetals (MoX_2 and WX_2) display semiconducting characteristic. Bulk TMDs show several polymorphs and stacking polytypes. 1T, 2H and 3R are the most common existent polymorphs of TMDs, where the letters (T, H, and R) represent Trigonal, Hexagonal, and Rhombohedral, respectively, and the digit specifies the number of X–M–X units in the unit cell shown in Figure S9b [81].

Among large family of transition metal dichalcogenides semiconducting groups, *VI* TMDs including MoS_2 and WS_2, with a sizeable band gap (~1eV), have attracted tremendous research interest. In addition to the extensive study of electronic properties, the investigation of photochemical properties of single-layer of group *VI* semiconducting TMDs is another fast developing research area. Consequently, several theoretical investigations have also indicated that monolayer MoS_2 can be a promising photocatalyst for solar water splitting to hydrogen evolution[82].

The band structure of bulk MoS_2 is reported experimentally and theoretically in different works. According to the published theoretical studies, like ab initio calculation, as well as experimental methods like angle-resolved photoelectron spectroscopy (ARPES), the band gap energy for trigonal prismatic structure of MoS_2 is indirect with a valence band maximum (VBM) at the Γ point and a conduction band minimum (CBM) at the midpoint along Γ–K symmetry lines. However, the exfoliated single layer of the same material is a direct band gap semiconductor with VBM and CBM coinciding at the K-point (Figure S9c). The band alignment of most TMDs (single/few layers TMDs) as well as MoS_2 is energetically favorable with respect to the redox potentials of water oxidation and proton reduction for solar assisted hydrogen generation from water (Figure S9d) [83].

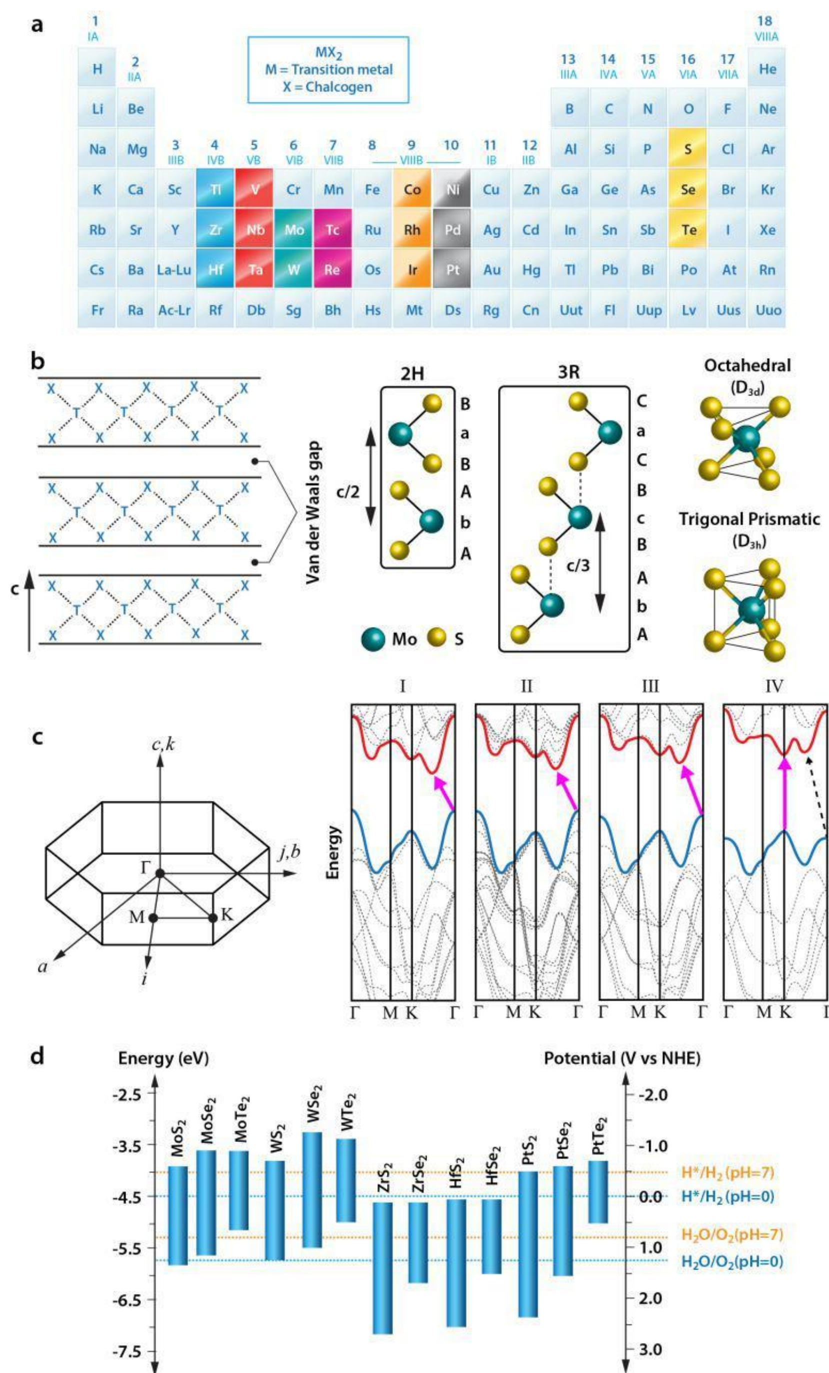

Figure S9 (a) Different types of existent layered TMD compounds. The transition metals and the three chalcogen highlighted elements in the periodic table, mainly form layered structures. Partially highlighted Co, Rh, Ir and Ni represent that only some of the dichalcogenides crystalized in layered structures. Reproduced with permission from Ref. [83]. Copyright 2013 Macmillan Publishers Ltd (b) Structural design in TMDs. The different coordination of the metal atoms is presented on the left and Stacking types for different layered chalcogenides along. Adapted with permission from Ref.[81]. Copyright 1988 Elsevier Science. (c)Layer dependent band structure of MoS_2. Reproduced with permission from Ref [83]. Copyright 2010 American Chemical Society (d) Band edge position of some of the single layers TMDs, calculated by means of DFT and the many-body GW approach. The horizontal orange dashed line represents the redox potential of water oxidation and H^+ reduction at pH = 7 and the blue dashed line represents at pH = 0. Reproduced with permission from Ref.[82]. Copyright 2010.KIM and Springer.

3.3 g-C_3N_4

Polymeric graphitic carbon nitride materials (g-C_3N_4 or GCN) which composed of C, N, and partial H content is the subject of intensive research in recent years due to their outstanding properties such as remarkable hardness, low friction coefficient and reliable chemical inertness [82]. Carbon nitrides have several allotropes including α, β , cubic, pseudocubic, and graphitic structures; Among these allotropes, the graphitic phase is reported as the most stable under ambient conditions. g-C_3N_4 has a layered 2D structure similar to graphite in which a nitrogen heteroatom is replaced by carbon atom in π-conjugated graphite framework. The inter layer distance of stacked sheets in g-C_3N_4 is d=0.326 nm [84].

Carbon nitrides could be synthesized by pyrolysis of nitrogen containing precursors following the self-condensation and the deammonation process of ammonocarbonic acids. The fabricated products, depending on the degree of condensation, are called melon (tri-s-triazines) or melamine (s-triazine units). According to density functional theory (DFT) predications, melon based structures are energetically stable as compared to melamine structures [84]. Hence, g-C_3N_4 framework is composed of tri-s-triazine and s-heptazine units (Figure S10a,b) [85]. It is worth nothing that the degree of condensation, which determines the number and configuration of lone pair electrons of nitrogen in carbon nitride polymer, has an essential role in the electronic and optical properties of g-C_3N_4 that can be determined by using DFT calculations. The computed band gap energy for melon is 2.07 eV (Figure S10c and the calculated valence band maximum (VBM) for g-C_3N_4 is found to be 1.4 V, below the water oxidation level, (Figure S10d) [86]. The conduction band minimum (CBM) of g-C_3N_4 is calculated at 1.3 V above the water reduction potential. Therefore, the g-C_3N_4 could be considered a promising photocatalyst for H_2 production in water splitting reaction [87].

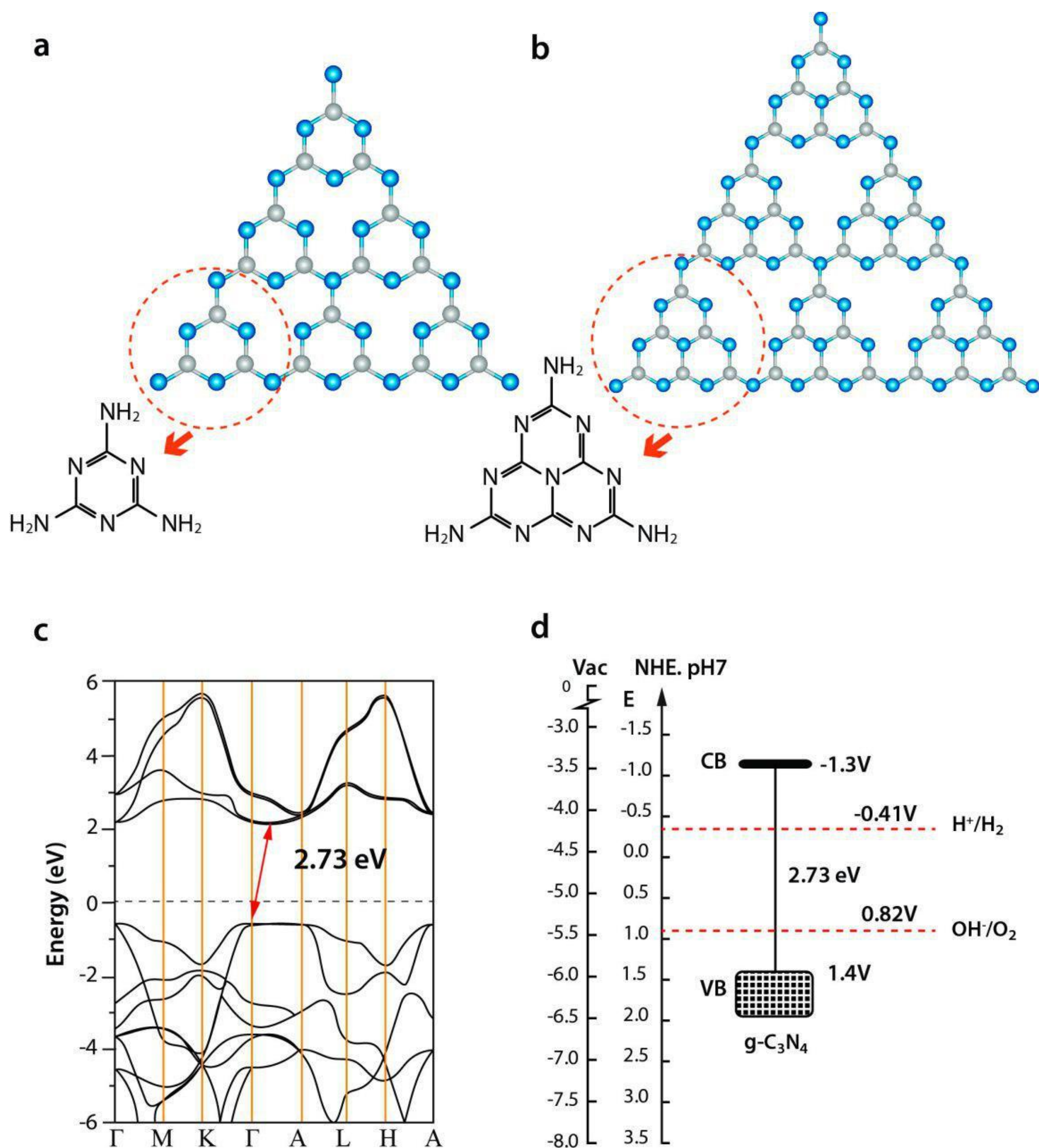

Figure S10 The schematic illustration of the (a) s-triazine and (b) s-heptazine unit structure. Reproduced and adapted with permission from Ref.[85]. Copyright 2014 Elsevier Science. (c) DFT calculated band structure for bulk g-C_3N_4 at the high symmetry points in the Brillouin Zone Reproduced with permission from. Ref. [86]. Copyright 2016 Elsevier and (d) band edge position of g-C_3N_4. The redox potential of water oxidation is indicated by the red dashed line and H^+ reduction to H_2 is indicated by the blue dashed line. Reproduced with permission from. Ref. [87]. Copyright 2012 American Chemical Society.

Table S1. graphene-based photocatalysts for H_2 production by water splitting

2D/ SC Photoelectrode	preparation method	Incident light (source P=mW/cm²) (λ nm)	Electrolyte	Bias (V)vs RHE	IPCE% (at λ (nm)- V vs. RHE))	Photocurrent density (mA/cm²)	H_2 production rate µmol/h.cm²	Ref
GR(1mg/mL)/ Cu_2O/Cu	Anodization/Immersion	Xe-1.5 AM-p=100c	1 M Na_2SO_4 pH 5 with K_3PO_4 0.1 M	0	N/A	4.8	N/A	[88]
GR/TiO_2 nanofiber	Doctor Blade method	Xe λ > 320	0.1M KOH	0.9	N/A	0.057	N/A	[56]
TiO_2/GR (TiO_2(100))	Doctor Blade method	UV- 365nm	0.5MNa_2SO_4	0.7	N/A	475	N/A	[89]
Fe_2O_3–(0.2wt%)GRNP	Spin coating	Xe- P=150	1 M NaOH	1	N/A	2.5	8000 at 0.6 V/SCE	[90]
TiO_2 NR/ N-doped GR/CdS	Solovothermal technique/ drop casting/successive ionic layer adsorption and reaction (SILAR) method	Xe- P=90	0.1 M NaOH	0.25	N/A	0.310	N/A	[91]
$Zn_{0.5}Cd_{0.5}S$ porous NS/(5wt%)RGO	Drop casting	Xe- λ>420	0.1M Na_2S and 0.1M Na_2SO_3	N/A	N/A	-	12.05 at 0.6 V/SCE	[92]
RGO/TiO_2	Anodization/Electrochemical deposition	Xe- 1.5 AM-P=100	1 M KOH	1.23	96.2% λ =350 V=1.23	1.44	N/A	[93]
CdS/GR	Layer-by-layer self-assembly	Xe- λ > 420AM 1.5	0.1 M Na_2S	0 V	N/A	0.025	N/A	[94]
CdS/RGO/TiO_2 NT	Anodization/Electrophoretic deposition / successive ionic layer adsorption and reaction (SILAR) method	Xe- λ>400,-P=100	1M KOH	0.25	N/A	0.105	N/A	[95]
$BiMo_{0.03}V_{0.97}O_4$/GR	Spin coating/Galvanostatic reduction deposition	Xe -λ>420 -P=200	0.1 M Na_2SO_4	1.24	50% at λ<440 V=1.23	3.5	N/A	[96]
NiO/rGO/TiO_2 p-n heterostructure	Dip coating	Xe-P=100	1 M NaOH	0.44	N/A	0.007	N/A	[97]
$BiVO_4$-RGO	Drop casting	Xe- λ>420	0.1 M Na_2SO_4	0.8 V	4.2% λ =420 V=0.95	0.070	0.5	[98]
Fe_2O_3-CNT/graphene	Electron beam evaporation/Spray coating	sun simulator-1.5 AM-P=100	1 M NaOH	1.23 V	N/A	325	N/A	[99]
RGO/$Zn_{1-x}Ag_xO$	Electrodeposition	Xe -1.5 AM- P=100	0.1 M NaOH	1	N/A	2.48	N/A	[100]

WO_3–RGO	Dip coating	Xe -1.5 AM- P=100	0.5 M H_2SO_4	1.24	N/A	1.1	6.75	[101]
Fe_2O_3/graphene	Hydrolysis solvothermal technique/Spin coating	Xe -λ>420 - P=100	1.0 M NaOH	1.5 V	18.6% λ= 400 V= 1.5	0.63	N/A	[102]
TiO_2/RGO/Cu_2O	Hydrothermal method/Spin coating/ Chemical solution deposition	Xe- P=100	0.5 M Na_2SO_4	0.55	55% λ=370–400	N/A	631.6	[103]
α-Fe_2O_3/GR inverse opal	Hydrothermal method/CVD	sun simulator- 1.5 AM	1 M NaOH	1.5	42% t λ= 320 V =0.5	1.62	N/A	[104]
N-doped GR/TiO_2	Coating/not av	Xe	0.5 M Na_2SO_4	0.7	N/A	0.007	N/A	[105]
Nb_2O_5-RGO(4wt%)	Drop casting	Xe	0.5 M Na_2SO_4	0.7	N/A	0.0286	N/A	[106]
Branched TiO_2/RGO/CdS	Spin coating/Solvothermal technique/Drop casting/successive ionic layer adsorption and reaction (SILAR) method	Xe P=90	0.1 M Na_2S	1	N/A	3	N/A	[107]
N-doped Nb_2O_5/RGO	Coating-not av	Xe -λ>420 P=300	0.1 M Na_2SO_4	1.9 V	N/A	0.0136	N/A	[108]
CdS/P25/GR aerogel	Spread	Xe -1.5 AM- P=100	0.24 M Na_2S 0.35 M Na_2SO_3	0.2	N/A	0.2	N/A	[109]
Bi_2S_3/rGO/TiO_2 NR	SILAR/Spin coating/Hydrothermal method	Xe λ>420 –P=300	0.35MNa_2SO_3 0.25MNa_2S	0.25	N/A	2	N/A	[110]
α-Fe_2O_3NR/GR/ $BiV_{1-x}Mo_xO_4$	Hydrothermal method/Spin coating/Spin coating	Xe-1.5 AM P=100	0.01M Na_2SO_4	0.2	N/A	0.85	N/A	[111]
ZnO HM/GR core - shell	Doctor Blade method	Xe -λ>400	0.1 M Na_2SO_4	1.24	N/A	0.15	N/A	[112]
ZnO triangle/GO	Hydrothermal method	UV light 360-nm	1.0M NaOH	1.23	10.41% λ= 360 V=1.23	1.29	N/A	[113]
N-deficient Porousg-C_3N_4 NS/ N-doped GR/NiFe	Hydrothermal method	Xe -1.5 AM P=100	0.01 M Na_2SO_4	1.22	2.5% λ= 350 V=1.22	0.0729	N/A	[114]
TiO_2/RGO	Doctor Blade method	Xe -1.5 AM P=100	0.5 M H_2SO_4	1.23	N/A	0.20	N/A	[115]
RGO/ZnO/RGO	Electrodeposition/Electrodeposition/ Electrodeposition	Xe -1.5 AM	0.1 M KOH	0.6	N/A	0 .928	N/A	[116]
$BiVO_4$/graphene/TiO_2	Spin coating/Dip coating	Xe -1.5 AM P=100	0.1M K_2SO_4	1	N/A	0.130	N/A	[11]

TiO_2Inverse opal@rGO@Au	Spin coating/immersion	Xe-1.5AM-100 mW /cm^2	0.5 M Na_2SO_4	1.23 V vs RHE	N/A	1.29	17.8 µmol/cm^2	[117]
Ag_3PO_4/3D graphene	Doctor blade method	Halogen lamp-150 W-λ>400 nm	0.02 M Na_3PO_4	0.5 V vs Ag/AgCl	N/A	2.5 µA/cm^2	N/A	[118]
RGO(4h immersion time)/Cu_2O/Cu	Chemical oxidation of a copper foil/Immersion	Halogen tungsten lamp-100 mW/cm^2	0.5 M Na_2SO_4	0 V vs. RHE	N/A	− 2.54 mA/cm^2	N/A	[119]
RGO/ZnO nanowire	Wet chemistry/Pulse sonication technique	Xe-1.5 AM-100 mW/cm^2	0.5M Na_2SO_4	1 V vs Ag/AgCl	N/A	1.55 mA/cm^2	N/A	[120]
GR=graphene NP=nanoplate	NR=nanorod NS=nanosheet	RGO=reduced graphene oxide		HM= hollow microsphere		Xe=xenon lamp P= lamp power		λ=wave length

Table S2. a summary of MS_2/semiconductor electrodes (M=Mo, W) for PEC hydrogen evolution

2D/ SC Photoelectrode	preparation method	Incident light (source P=mW/cm^2) (λ nm)	Electrolyte	Bias (V)	Solar Hydrogen evolution efficiency: IPCE%	Photocurrent density (mA/cm^2)	H_2 production rate	Ref
1D/2D nearly vertical CdS/MoS_2 heterostructures	glucose-assisted hydrothermal reaction	300W Xenon arc lamp (λ > 420 nm, 160 mW/cm^2)	0.35 M/0.25 M Na_2S–Na_2SO_3	0		0.025	10 mmol/g/h	121
CdSe QD/WS_2 nanosheet	Ultrasonication-hydrothermal	300W Xenon arc lamp (λ > 420 nm, 160 mW/cm^2	Na_2SO_4 0.5 M			1.21	14 mmol/h	122
MoS_2/Si	photoreduction method	Xe lamp (100 mW/cm2)	1 M $HClO_4$	-0.35		34.5		123
MoS_2/g-C_3N_4	impregnation-sulphidation	Xenon 300 W lamp	KCl 3 M	0		0.015		124
MoS_2 / Porphyrins	Li intercalation	150 W Xenon lamp (λ>400 nm)	10 mM ascorbate	0.2		0.001		125
MoS_2 / $CuInS_2$	two-step hydrothermal	(λ>550 nm)	0.5 M Na_2SO_4	--		0.008		126
MoS_2/S-Doped g-C_3N_4	CVD and Hydrothermal	150 W Xenon lamp (λ>420 nm)	0.1 M Na_2SO_4	0.5		0.12		21
MoS_2/CdS	solvothermal	(λ>420 nm)	Lactic acid	---		0.04		127
$Zn_{0.5}Cd_{0.5}S$ Nanorods@MoS_2/RGO	simultaneous reduction reaction	Visible light	$NaSO_3$/Na_2S	0.3		0.4		128
WS_2/CdS	Exfoliation-SILAR	500 W Xe lamp	50 mM Na_2S	0.1		0.35		129
MoS_2/CdS	Exfoliation-SILAR	500 W Xe lamp	50 mM Na_2S	0.1		0.28		30
MoS_2–TiO_2	Ball milling	300 W Xe lamp (λ>380 nm)	0.1 M Na_2SO_4	0.0		0.1		130
MoS_2 / C_3N_4	In situ light-assisted method.	300 W Xe lamp (λ>400 nm)	hexamethylene tetramine and HCl	-0.22		0.06		131
MoS_2-TiO_2	hydrothermal reaction	300 W xenon arc lamp λ=320–780 nm	0.35 M Na_2S and 0.25 M Na_2SO_3	0.0		0.1		132

WS_2@MoS_2	Ball milling-solvothermal	500 W Xe lamp (λ>400 nm)	0.1 M Na_2SO	--		0.15	[133]
$In_2S_3/MoS_2/$ CdS	hydrothermal	300 W Xe lamp (λ>420 nm)	0.1 M Na_2SO	--		0.25	[134]
MoS_2/TiO_2/graphene	one-pot hydrothermal	350 W Xe arc lamp	Na_2S and Na_2SO_3	0.6		2.5	[135]
2D MoS_2/CdS p–n nanohybrids	one-pot solvothermal	0.5 Sun (50 mWcm-2).	0.5 M Na_2SO_4	---		0.23	[136]
MoS_2/CdS p-n heterojunction	electrodeposition and chemical bath deposition	300 W Xe lamp (λ>420 nm)	0.50 M Na_2S/Na_2SO_3	0.0	28% at 420 nm	28	[137]
MoS_2-C_3N_4	Impregnation and hydrotherma	300 W Xe lamp (λ>420 nm)	0.01M Na_2SO_4	---		0.015	[138]
TiO_2–MoS_2(1T)	self-assembly method	300 W Xe lamp (λ<400 nm, UV light)	----	0.0		0.03	[139]
p-type Cu_2O/MoS_2 nanosheets	Hydrothermal participation	Xe lamp (λ=480 nm)	5% (v/v) methanol + Na_2SO_4	-0.1		0.17	[140]
bulk heterojunctions of MoS_2 and WS_2 nanosheets	redox reaction of Li intercalated MoS_2 and WS_2 powders in water	Hg Lamp	0.5M $NaClO_4$ solution	+1		0.45	[141]
Xe=xenon lamp P= lamp power	λ=wave length						

2D/ SC Photoelectrode	preparation method	Incident light (source P=mW/cm^2) (λ nm)	Electrolyte	Bias (V)	IPCE%	Photocurrent density (mA/cm^2)	H_2 production rate µmol/h.cm^2	Ref
Table S3. The effect of various GCN interface structures on PEC and PC H_2 production								
$g-C_3N_4-Pt-TiO_2$	Pyrolysis/Chemical adsorption	λ> 420	1 M Na_2SO_4	N/A	N/A	~ 0.06	178 µmol/h	[142]
au-PtO/$g-C_3N_4$	thermal treatment/photodeposition	λ> 400	0.5 M Na_2SO_4	N/A	N/A	NA	16.9µmol/h	[143]
ZnS microsphere/$g-C_3N_4$	Precipitation	LED 420	0.2 M Na_2SO_4	N/A	N/A	NA	194 µmol/hg	[144]
CdS/$g-C_3N_4$	thermal Polymerization/precipitation	λ> 420	N/A	N/A	N/A	~0.25 µA/cm^2	601µmol/h	[145]
CdS/$g-C_3N_5$	Solvothermal/Chemisorption	λ> 420	(0.35 M Na_2S + 0.25 M Na_2SO_3) and 0.5 M Na_2SO_4	0 V vs Ag/AgCl	N/A	~ 0.04 mA/cm^2	4152 µmol/hgr	[146]
CdS QD/$g-C_3N_6$	Chemical imperegnation	λ> 400	0.01 M Na_2SO_4	N/A	N/A	~0.0017 mA/cm^2	17.27µmol/h	[147]
$MoS_2-g-C_3N_4$	Chemical imperegnation	λ> 420	0.01 M Na_2SO_4	0.5 V vs Ag/AgCl	N/A	~ 0.01 mA/cm^2	23.1µmol/h	[138]
$g-C_3N_4/Fe_2O_3$	Electrodeposition/CVD	300 W Xe λ> 400	1M NaOH	0.23 V vs Ag/AgCl	1.5 % at 420 nm and 0.4 V	~0.75 mA/cm^2	N/A	[148]
$g-C_3N_4$/N doped $SrTiO_3$	Polymeric citrate/Thermal exfoliation	300 W Xe 700> λ> 400	0.1 M Na_2SO_4	N/A	N/A	~ 0.4 mA/cm^2	N/A	[149]
$V_2O_5/g-C_3N_4$	In situ growth	250 W Xe λ> 420	N/A	N/A	N/A	~ 0.12 µA/cm^2	N/A	[150]
TiO_2-In_2O3@$g-C_3N_4$	Solvothermal	500 W Xe	0.1 M Na_2SO_4	0.1 V	N/A	~ 0.7 µA	~ 8.6 µmol/h	[151]
3D $CoO_x/g-C_3N_4$/Ba-TaON	Hydrothermal/exfoliation	Sun Simulator	1 M NaOH	1.23 V RHE	N/A	4.57 mA/cm^1	~ 52 µmol/hcm^2	[152]
Zn-tri-PcNc/$g-C_3N_4$	Impregnation	300 W Xe λ> 420 and 500 nm	2 M NaOH	N/A	N/A	N/A	125.2µmol/h	[153]
$g-C_3N_4/CuInS_2$	Thermal polycondensation	300 W Xe λ> 420 , AM 1.5	0.1 M H_2SO_4	0.36 V vs RHE	N/A	250µA/cm^2	N/A	[154]

Xe=xenon lamp
P= lamp power

References

1. M. G. R Van de Krol, *Photoelectrochemical Hydrogen Production*, Springer, 2012.
2. G. Wang, Y. Ling, H. Wang, L. Xihong and Y. Li, *J. Photochem. Photobiol. C Photochem. Rev.*, 2014, **18**, 35-51.
3. B. Seger, I. E. Castelli, P. C. K. Vesborg, K. W. Jacobsen, O. Hansen and I. Chorkendorff, *Energy Environ. Sci.*, 2014, **7**, 2397-2413.
4. M. Zhou, X. W. Lou and Y. Xie, *Nano Today*, 2013, **8**, 598-618.
5. Y. Li and J. Z. Zhang, *Laser & Photonics Reviews*, 2010, **4**, 517-528.
6. M. G. Walter, E. L. Warren, J. R. McKone, S. W. Boettcher, Q. Mi, E. A. Santori and N. S. Lewis, *Chemical reviews*, 2010, **110**, 6446-6473.
7. M. Grätzel, *Nature*, 2001, **414**, 338-344.
8. J. Li, B. Shen, Z. Hong, B. Lin, B. Gao and Y. Chen, *Chem. Commun.*, 2012, **48**, 12017-12019.
9. Z. Li, W. Luo, M. Zhang, J. Feng and Z. Zou, *Energy Environ. Sci.*, 2013, **6**, 347-370.
10. J. Hu, H. Li, Q. Wu, Y. Zhao and Q. Jiao, *Chem. Eng. J.*, 2015, **263**, 144-150.
11. S. Yousefzadeh, M. Faraji and A. Z. Moshfegh, *Journal of Electroanalytical Chemistry*, 2016, **763**, 1-9.
12. W.-Y. Yan, Q. Zhou, X. Chen, Y. Yang, Y. Zhang, X.-J. Huang and Y.-C. Wu, *Journal of hazardous materials*, 2016, **314**, 41-50.
13. S. Yousefzadeh, M. Faraji, Y. T. Nien and A. Z. Moshfegh, *Appl Surf Sci*, 2014, **320**, 772-779.
14. H. Y. Abbasi, A. Habib and M. Tanveer, *J Alloys Compd*, 2017, **690**, 21-26.
15. A. Pruna, Q. Shao, M. Kamruzzaman, J. Zapien and A. Ruotolo, *Ceramics International*, 2016, **42**, 17192-17201.
16. A. Nourmohammadi, R. Rahighi, O. Akhavan and A. Moshfegh, *J Alloys Compd*, 2014, **612**, 380-385.
17. M. Ebrahimi, M. Samadi, S. Yousefzadeh, M. Soltani, A. Rahimi, T.-c. Chou, L.-C. Chen, K.-H. Chen and A. Z. Moshfegh, *ACS Sustainable Chemistry & Engineering*, 2016, **5**, 367–375.
18. X. Zhang, Q. Zhang, Y. Sun, P. Zhang, X. Gao, W. Zhang and J. Guo, *Electrochim Acta*, 2016, **189**, 224-230.
19. Y.-J. Yuan, J.-R. Tu, Z.-J. Ye, D.-Q. Chen, B. Hu, Y.-W. Huang, T.-T. Chen, D.-P. Cao, Z.-T. Yu and Z.-G. Zou, *Appl. Catal. B Environ.*, 2016, **188**, 13-22.
20. H. Li, Y. Wang, G. Chen, Y. Sang, H. Jiang, J. He, X. Li and H. Liu, *Nanoscale*, 2016, **8**, 6101-6109.
21. L. Ye, D. Wang and S. Chen, *ACS Appl Mater Interfaces*, 2016, **8**, 5280-5289.
22. X. Song, Y. Hu, M. Zheng and C. Wei, *Appl. Catal. B Environ.*, 2016, **182**, 587-597.
23. L. Wang, Z. Xu, W. Wang and X. Bai, *J. Am. Chem. Soc.*, 2014, **136**, 6693-6697.
24. H. Du, H. L. Guo, Y. N. Liu, X. Xie, K. Liang, X. Zhou, X. Wang and A. W. Xu, *ACS Appl. Mater. Interfaces*, 2016, **8**, 4023-4030.
25. Y.-J. Yuan, Z.-J. Ye, H.-W. Lu, B. Hu, Y.-H. Li, D.-Q. Chen, J.-S. Zhong, Z.-T. Yu and Z.-G. Zou, *ACS Catal.*, 2016, **6**, 532-541.
26. G. Binnig, C. F. Quate and C. Gerber, *Phys Rev Lett*, 1986, **56**, 930.
27. H. Li, X. Qi, J. Wu, Z. Zeng, J. Wei and H. Zhang, *ACS Nano*, 2013, **7**, 2842-2849.
28. Z. Zeng, Z. Yin, X. Huang, H. Li, Q. He, G. Lu, F. Boey and H. Zhang, *Angewandte Chemie International Edition*, 2011, **50**, 11093-11097.
29. Z. Zeng, T. Sun, J. Zhu, X. Huang, Z. Yin, G. Lu, Z. Fan, Q. Yan, H. H. Hng and H. Zhang, *Angewandte Chemie International Edition*, 2012, **51**, 9052-9056.
30. M. Zirak, M. Ebrahimi, M. Zhao, O. Moradlou, M. Samadi, A. Bayat, H. L. Zhang and A. Z. Moshfegh, *RSC Adv.*, 2016, **6**, 16711-16719.

31. H. Li, Z. Yin, Q. He, H. Li, X. Huang, G. Lu, D. W. H. Fam, A. I. Y. Tok, Q. Zhang and H. Zhang, *Small*, 2012, **8**, 63-67.
32. S. Yang, Y. Gong, J. Zhang, L. Zhan, L. Ma, Z. Fang, R. Vajtai, X. Wang and P. M. Ajayan, *Adv Mater*, 2013, **25**, 2452-2456.
33. T. Lopes, L. Andrade, H. A. Ribeiro and A. Mendes, *Int J Hydrogen Energy*, 2010, **35**, 11601-11608.
34. X. Wang, K. Maeda, A. Thomas, K. Takanabe, G. Xin, J. M. Carlsson, K. Domen and M. Antonietti, *Nat Mater*, 2009, **8**, 76-80.
35. Q. Lin, L. Li, S. Liang, M. Liu, J. Bi and L. Wu, *Appl. Catal. B Environ.*, 2015, **163**, 135-142.
36. F. T. Johra, J.-W. Lee and W.-G. Jung, *Journal of Industrial and Engineering Chemistry*, 2014, **20**, 2883-2887.
37. L. Malard, M. Pimenta, G. Dresselhaus and M. Dresselhaus, *Physics Reports*, 2009, **473**, 51-87.
38. M. A. Pimenta, E. del Corro, B. R. Carvalho, C. Fantini and L. M. Malard, *Accounts of Chemical Research*, 2014, **48**, 41-47.
39. Z. Ni, Y. Wang, T. Yu and Z. Shen, *Nano. Res.*, 2008, **1**, 273-291.
40. J. Zheng, H. Zhang, S. Dong, Y. Liu, C. T. Nai, H. S. Shin, H. Y. Jeong, B. Liu and K. P. Loh, *Nature communications*, 2014, **5**, 2995.
41. C. Lee, H. Yan, L. E. Brus, T. F. Heinz, J. Hone and S. Ryu, *ACS Nano*, 2010, **4**, 2695-2700.
42. J. W. Rabalais, *Principles of Ultraviolet Photoelectron Spectroscopy*, Wiley, 1976.
43. S. Giménez and J. Bisquert, *Photoelectrochemical Solar Fuel Production*, Springer, 2016.
44. R. Koolstra, University of Twente, 2015.
45. J. Tauc, *Materials Research Bulletin*, 1968, **3**, 37-46.
46. J. L. M. L. Bergman, *Handbook of Luminescent Semiconductor Materials*, CRC Press, 2011.
47. J. R. Albani, *Principles and applications of fluorescence spectroscopy*, John Wiley & Sons, 2008.
48. S. Berger, C. Voisin, G. Cassabois, C. Delalande, P. Roussignol and X. Marie, *Nano Lett.*, 2007, **7**, 398-402.
49. L. Vayssieres, *On Solar Hydrogen and Nanotechnology*, John Wiley & Sons, 2010.
50. M. Radecka, M. Wierzbicka, S. Komornicki and M. Rekas, *Phys B: Condens Matter*, 2004, **348**, 160-168.
51. N. Naseri, M. Qorbani, H. Kim, W. Choi and A. Moshfegh, *J. Phys. Chem. C*, 2015, **119**, 1271-1279.
52. Z. Chen, H. N. Dinh and E. Miller, *SpringerBriefs in Energy, New York*, 2013, 49-61.
53. A. Zaban, M. Greenshtein and J. Bisquert, *ChemPhysChem*, 2003, **4**, 859-864.
54. D. Monllor-Satoca and R. Gómez, *J. Phys. Chem. C*, 2008, **112**, 139-147.
55. K. Sivula and R. Van De Krol, *Nature Reviews Materials*, 2016, **1**, 15010.
56. H. I. Kim, S. Kim, J. K. Kang and W. Choi, *J. Catal.*, 2014, **309**, 49-57.
57. S. Jo, P. Verma, Y. Kuwahara, K. Mori, W. Choi and H. Yamashita, *J. Mater. Chem. A*, 2017, **5**, 21883-21892.
58. K. Gelderman, L. Lee and S. W. Donne, *Journal of Chemical Education*, 2007, **84**, 685.
59. Z. Chen, T. G. Deutsch, H. N. Dinh, K. Domen, K. Emery, A. J. Forman, N. Gaillard, R. Garland, C. Heske and T. F. Jaramillo, in *Photoelectrochemical Water Splitting*, Springer, 2013, pp. 63-85.
60. L. Wang, R. Long and O. V. Prezhdo, in *Annual Review of Physical Chemistry*, Annual Reviews Inc., 2015, pp. 549-579.
61. T. L. Bahers, M. Rérat and P. Sautet, *J. Phys. Chem. C*, 2014, **118**, 5997-6008.
62. L. Xu, W. Q. Huang, L. L. Wang, G. F. Huang and P. Peng, *J. Phys. Chem. C*, 2014, **118**, 12972-12979.
63. Y. Peter and M. Cardona, *Fundamentals of Semiconductors: Physics and Materials Properties*, Springer Science & Business Media, 2010.

64. R. Long, N. J. English and O. V. Prezhdo, *J. Am. Chem. Soc.*, 2012, **134**, 14238-14248.
65. H. Zhang, Y. N. Zhang, H. Liu and L. M. Liu, *J. Mater. Chem. A*, 2014, **2**, 15389-15395.
66. M. C. Toroker, D. K. Kanan, N. Alidoust, L. Y. Isseroff, P. Liao and E. A. Carter, *Phys. Chem. Chem. Phys.*, 2011, **13**, 16644-16654.
67. B. C. Brodie, *Philosophical Transactions of the Royal Society of London*, 1859, **149**, 249-259.
68. G. R. Bhimanapati, Z. Lin, V. Meunier, Y. Jung, J. Cha, S. Das, D. Xiao, Y. Son, M. S. Strano and V. R. Cooper, *ACS Nano*, 2015, **9**, 11509-11539.
69. K. S. Novoselov, A. K. Geim, S. Morozov, D. Jiang, Y. Zhang, S. a. Dubonos, I. Grigorieva and A. Firsov, *Science*, 2004, **306**, 666-669.
70. A. C. Neto, F. Guinea, N. Peres, K. S. Novoselov and A. K. Geim, *Reviews of Modern Physics*, 2009, **81**, 109.
71. G. Lu, K. Yu, Z. Wen and J. Chen, *Nanoscale*, 2013, **5**, 1353-1368.
72. A. Politano and G. Chiarello, *Nanoscale*, 2014, **6**, 10927-10940.
73. P. Avouris, *Nano Lett.*, 2010, **10**, 4285-4294.
74. J. Yao, Y. Sun, M. Yang and Y. Duan, *J. Mater. Chem.*, 2012, **22**, 14313-14329.
75. G. Xie, K. Zhang, B. Guo, Q. Liu, L. Fang and J. R. Gong, *Adv Mater*, 2013, **25**, 3820-3839.
76. T. S. Sreeprasad and V. Berry, *Small*, 2013, **9**, 341-350.
77. M. Pykal, P. Jurečka, F. Karlický and M. Otyepka, *Phys. Chem. Chem. Phys.*, 2016.
78. M. Chhowalla, H. S. Shin, G. Eda, L.-J. Li, K. P. Loh and H. Zhang, *Nature Chemistry*, 2013, **5**, 263-275.
79. X. Duan, C. Wang, A. Pan, R. Yu and X. Duan, *Chem. Soc. Rev.*, 2015, **44**, 8859-8876.
80. M. Samadi, N. Sarikhani, M. Zirak, H. Zhang, H.-L. Zhang and A. Z. Moshfegh, *Nanoscale Horizons*, 2018, **3**, 90-204.
81. W. Jaegermann and H. Tributsch, *Progress in Surface Science*, 1988, **29**, 1-167.
82. D. M. Andoshe, J. M. Jeon, S. Y. Kim and H. W. Jang, *Electron. Mater. Lett.*, 2015, **11**, 323-335.
83. A. Splendiani, L. Sun, Y. Zhang, T. Li, J. Kim, C.-Y. Chim, G. Galli and F. Wang, *Nano Lett.*, 2010, **10**, 1271-1275.
84. in *5th KKU International Engineering Conference 2014, KKU-IENC 2014*, Trans Tech Publications, Khon Kaen, 2014.
85. G. Dong, Y. Zhang, Q. Pan and J. Qiu, *J. Photochem. Photobiol. C Photochem. Rev.*, 2014, **20**, 33-50.
86. J. Liu, *J Alloys Compd*, 2016, **672**, 271-276.
87. X. Wang, S. Blechert and M. Antonietti, *ACS Catal.*, 2012, **2**, 1596-1606.
88. A. A. Dubale, W. N. Su, A. G. Tamirat, C. J. Pan, B. A. Aragaw, H. M. Chen, C. H. Chen and B. J. Hwang, *J. Mater. Chem. A*, 2014, **2**, 18383-18397.
89. L. Liu, Z. Liu, A. Liu, X. Gu, C. Ge, F. Gao and L. Dong, *ChemSusChem*, 2014, **7**, 618-626.
90. S. Rai, A. Ikram, S. Sahai, S. Dass, R. Shrivastav and V. R. Satsangi, *RSC Adv.*, 2014, **4**, 17671-17679.
91. J. Selvaraj, S. Gupta, S. Delacruz and V. Subramanian, *ChemPhysChem*, 2014, **15**, 2010-2018.
92. J. Zhang, W. Zhao, Y. Xu, H. Xu and B. Zhang, *Int J Hydrogen Energy*, 2014, **39**, 702-710.
93. X. Zhang, B. Zhang, D. Huang, H. Yuan, M. Wang and Y. Shen, *Carbon*, 2014, **80**, 591-598.
94. F.-X. Xiao, J. Miao and B. Liu, *J. Am. Chem. Soc.*, 2014, **136**, 1559-1569.
95. H. Li, Z. Xia, J. Chen, L. Lei and J. Xing, *Appl. Catal. B Environ.*, 2015, **168-169**, 105-113.

96. W. Li, J. Yue, Y. Bu and Z. Chen, *RSC Adv.*, 2015, **5**, 77823-77830.
97. X. Yu, J. Zhang, Z. Zhao, W. Guo, J. Qiu, X. Mou, A. Li, J. P. Claverie and H. Liu, *Nano Energy*, 2015, **16**, 207-217.
98. Y. H. Ng, A. Iwase, A. Kudo and R. Amal, *J. Phys. Chem. Lett.*, 2010, **1**, 2607-2612.
99. J. Young Kim, J. W. Jang, D. Hyun Youn, J. Yul Kim, E. Sun Kim and J. Sung Lee, *RSC Adv.*, 2012, **2**, 9415-9422.
100. S. Upadhyay, S. Bagheri and S. B. Abd Hamid, *Int J Hydrogen Energy*, 2014, **39**, 11027-11034.
101. J. Lin, P. Hu, Y. Zhang, M. Fan, Z. He, C. K. Ngaw, J. S. C. Loo, D. Liao and T. T. Y. Tan, *RSC Adv.*, 2013, **3**, 9330-9336.
102. Q. Wu, J. Zhao, K. Liu, H. Wang, Z. Sun, P. Li and S. Xue, *Int J Hydrogen Energy*, 2015, **40**, 6763-6770.
103. W. Fan, X. Yu, H. C. Lu, H. Bai, C. Zhang and W. Shi, *Appl. Catal. B Environ.*, 2016, **181**, 7-15.
104. K. Y. Yoon, J. S. Lee, K. Kim, C. H. Bak, S. I. Kim, J. B. Kim and J. H. Jang, *ACS Appl. Mater. Interfaces*, 2014, **6**, 22634-22639.
105. Z. Mou, Y. Wu, J. Sun, P. Yang, Y. Du and C. Lu, *ACS Appl. Mater. Interfaces*, 2014, **6**, 13798-13806.
106. Z. Yue, D. Chu, H. Huang, J. Huang, P. Yang, Y. Du, M. Zhu and C. Lu, *RSC Adv.*, 2015, **5**, 47117-47124.
107. P. Pathak, S. Gupta, K. Grosulak, H. Imahori and V. Subramanian, *J. Phys. Chem. C*, 2015, **119**, 7543-7553.
108. M. Qamar, M. Abdalwadoud, M. I. Ahmed, A. M. Azad, B. Merzougui, S. Bukola, Z. H. Yamani and M. N. Siddiqui, *ACS Appl. Mater. Interfaces*, 2015, **7**, 17954-17962.
109. W. Han, L. Ren, L. Gong, X. Qi, Y. Liu, L. Yang, X. Wei and J. Zhong, *ACS Sustainable Chem. Eng.*, 2014, **2**, 741-748.
110. X. Wang, J. Xie and C. M. Li, *J. Mater. Chem. A*, 2015, **3**, 1235-1242.
111. Y. Hou, F. Zuo, A. Dagg and P. Feng, *Nano Lett.*, 2012, **12**, 6464-6473.
112. S. Bera, A. Naskar, M. Pal and S. Jana, *RSC Adv.*, 2016, **6**, 36058-36068.
113. S. Chandrasekaran, J. S. Chung, E. J. Kim and S. H. Hur, *Chem. Eng. J.*, 2016, **290**, 465-476.
114. Y. Hou, Z. Wen, S. Cui, X. Feng and J. Chen, *Nano Lett.*, 2016, **16**, 2268-2277.
115. A. Morais, C. Longo, J. R. Araujo, M. Barroso, J. R. Durrant and A. F. Nogueira, *Phys. Chem. Chem. Phys.*, 2016, **18**, 2608-2616.
116. S. J. Teh, C. W. Lai and S. B. A. Hamid, *Journal of Energy Chemistry*, 2016, **25**, 336-344.
117. R. Boppella, S. T. Kochuveedu, H. Kim, M. J. Jeong, F. Marques Mota, J. H. Park and D. H. Kim, *ACS Appl. Mater. Interfaces*, 2017, **9**, 7075-7083.
118. C. Cui, S. Li, Y. Qiu, H. Hu, X. Li, C. Li, J. Gao and W. Tang, *Appl. Catal. B Environ.*, 2017, **200**, 666-672.
119. Y. Ghayeb, M. M. Momeni and M. Menati, *J Mater Sci Mater Electron*, 2017, **28**, 7650-7659.
120. I. Khan, A. A. M. Ibrahim, M. Sohail and A. Qurashi, *Ultrasonics Sonochemistry*, 2017, **37**, 669-675.
121. Y. Li, L. Wang, T. Cai, S. Zhang, Y. Liu, Y. Song, X. Dong and L. Hu, *Chem. Eng. J.*, 2017, **321**, 366-374.
122. Y. Zhong, Y. Shao, F. Ma, Y. Wu, B. Huang and X. Hao, *Nano Energy*, 2017, **31**, 84-89.
123. J. Zhou, S. Dai, W. Dong, X. Su, L. Fang, F. Zheng, X. Wang and M. Shen, *Appl Phys Lett*, 2016, **108**, 213905.
124. D. Zheng, G. Zhang, Y. Hou and X. Wang, *Appl. Catal. A: Gen.*, 2016, **521**, 2-8.
125. H. Zhang, J. Choi, A. Ramani, D. Voiry, S. N. Natoli, M. Chhowalla, D. R. McMillin and J. H. Choi, *ChemPhysChem*, 2016, **17**, 2854-2862.
126. Y. J. Yuan, D. Q. Chen, Y. W. Huang, Z. T. Yu, J. S. Zhong, T. T. Chen, W. G. Tu, Z. J. Guan, D. P. Cao and Z. G. Zou, *ChemSusChem*, 2016, **9**, 1003-1009.

127. J. He, L. Chen, F. Wang, Y. Liu, P. Chen, C. T. Au and S. F. Yin, *ChemSusChem*, 2016, **9**, 624-630.
128. S. N. Guo, Y. L. Min, J. C. Fan and Q. J. Xu, *ACS Appl Mater Interfaces*, 2016, **8**, 2928-2934.
129. M. Zirak, M. Zhao, O. Moradlou, M. Samadi, N. Sarikhani, Q. Wang, H.-L. Zhang and A. Moshfegh, *Sol Energ Mater Sol Cells*, 2015, **141**, 260-269.
130. Y. Zhu, Q. Ling, Y. Liu, H. Wang and Y. Zhu, *Phys. Chem. Chem. Phys.*, 2015, **17**, 933-940.
131. H. Zhao, Y. Dong, P. Jiang, H. Miao, G. Wang and J. Zhang, *J. Mater. Chem. A*, 2015, **3**, 7375-7381.
132. C. Liu, L. Wang, Y. Tang, S. Luo, Y. Liu, S. Zhang, Y. Zeng and Y. Xu, *Appl. Catal. B: Environ.*, 2015, **164**, 1-9.
133. H. Li, K. Yu, C. Li, B. Guo, X. Lei, H. Fu and Z. Zhu, *J. Mater. Chem. A*, 2015, **3**, 20225-20235.
134. W. Jiang, Y. Liu, R. Zong, Z. Li, W. Yao and Y. Zhu, *J. Mater. Chem. A*, 2015, **3**, 18406-18412.
135. W. Han, C. Zang, Z. Huang, H. Zhang, L. Ren, X. Qi and J. Zhong, *Int J Hydrogen Energy*, 2014, **39**, 19502-19512.
136. J. Zhang, Z. Zhu and X. Feng, *Chem. Eur. J.*, 2014, **20**, 10632-10635.
137. Y. Liu, Y. X. Yu and W. D. Zhang, *J. Phys. Chem. C*, 2013, **117**, 12949-12957.
138. L. Ge, C. Han, X. Xiao and L. Guo, *Int J Hydrogen Energy*, 2013, **38**, 6960-6969.
139. S. Bai, L. Wang, X. Chen, J. Du and Y. Xiong, *Nano. Res.*, 2014, **8**, 175-183.
140. Y. F. Zhao, Z. Y. Yang, Y. X. Zhang, L. Jing, X. Guo, Z. Ke, P. Hu, G. Wang, Y. M. Yan and K. N. Sun, *J. Phys. Chem. C*, 2014, **118**, 14238-14245.
141. F. M. Pesci, M. S. Sokolikova, C. Grotta, P. C. Sherrell, F. Reale, K. Sharda, N. Ni, P. Palczynski and C. Mattevi, *ACS Catal.*, 2017, **7**, 4990-4998.
142. B. Chai, T. Peng, J. Mao, K. Li and L. Zan, *Phys. Chem. Chem. Phys.*, 2012, **14**, 16745-16752.
143. J. Jiang, J. Yu and S. Cao, *Journal of Colloid and Interface Science*, 2016, **461**, 56-63.
144. F. Shi, L. Chen, C. Xing, D. Jiang, D. Li and M. Chen, *RSC Adv.*, 2014, **4**, 62223-62229.
145. D. Zheng, G. zhang and X. Wang, *Appl. Catal. B: Environ.*, 2015, **179**, 479-488.
146. J. Zhang, Y. Wang, J. Jin, J. Zhang, Z. Lin, F. Huang and J. Yu, *ACS Appl. Mater. Interfaces*, 2013, **5**, 10317-10324.
147. L. Ge, F. Zuo, J. Liu, Q. Ma, C. Wang, D. Sun, L. Bartels and P. Feng, *J. Phys. Chem. C*, 2012, **116**, 13708-13714.
148. Y. Liu, Y. X. Yu and W. D. Zhang, *Int J Hydrogen Energy*, 2014, **39**, 9105-9113.
149. S. Kumar, S. Tonda, A. Baruah, B. Kumar and V. Shanker, *Dalton Transactions*, 2014, **43**, 16105-16114.
150. Y. Hong, Y. Jiang, C. Li, W. Fan, X. Yan, M. Yan and W. Shi, *Appl. Catal. B: Environ.*, 2016, **180**, 663-673.
151. Z. Jiang, D. Jiang, Z. Yan, D. Liu, K. Qian and J. Xie, *Appl. Catal. B: Environ.*, 2015, **170-171**, 195-205.
152. J. Hou, H. Cheng, O. Takeda and H. Zhu, *Energy Environ. Sci.*, 2015, **8**, 1348-1357.
153. X. Zhang, L. Yu, C. Zhuang, T. Peng, R. Li and X. Li, *ACS Catal.*, 2014, **4**, 162-170.
154. F. Yang, V. Kuznietsov, M. Lublow, C. Merschjann, A. Steigert, J. Klaer, A. Thomas and T. Schedel-Niedrig, *J. Mater. Chem. A*, 2013, **1**, 6407-6415.